AGU PUBLICATIONS

JGR

Journal of Geophysical Research: Solid Earth

RESEARCH ARTICLE
10.1002/2014JB011736

Key Points:
- A model is developed to grow a fracture pattern under a self-referencing scheme
- Stress and scale dependency of fracture attributes is realistically modeled
- Permeability scaling behavior and flow structure transition are studied

Correspondence to:
Q. Lei,
q.lei12@imperial.ac.uk

Citation:
Lei, Q., J.-P. Latham, C.-F. Tsang, J. Xiang, and P. Lang (2015), A new approach to upscaling fracture network models while preserving geostatistical and geomechanical characteristics, *J. Geophys. Res. Solid Earth*, *120*, doi:10.1002/2014JB011736.

Received 30 OCT 2014
Accepted 4 JUN 2015
Accepted article online 6 JUN 2015

A new approach to upscaling fracture network models while preserving geostatistical and geomechanical characteristics

Qinghua Lei[1], John-Paul Latham[1], Chin-Fu Tsang[2,3], Jiansheng Xiang[1], and Philipp Lang[1]

[1]Department of Earth Science and Engineering, Imperial College London, London, UK, [2]Department of Earth Sciences, Uppsala University, Uppsala, Sweden, [3]Earth Sciences Division, Lawrence Berkeley National Laboratory, Berkeley, California, USA

Abstract A new approach to upscaling two-dimensional fracture network models is proposed for preserving geostatistical and geomechanical characteristics of a smaller-scale "source" fracture pattern. First, the scaling properties of an outcrop system are examined in terms of spatial organization, lengths, connectivity, and normal/shear displacements using fractal geometry and power law relations. The fracture pattern is observed to be nonfractal with the fractal dimension $D \approx 2$, while its length distribution tends to follow a power law with the exponent $2 < a < 3$. To introduce a realistic distribution of fracture aperture and shear displacement, a geomechanical model using the combined finite-discrete element method captures the response of a fractured rock sample with a domain size $L = 2$ m under in situ stresses. Next, a novel scheme accommodating discrete-time random walks in recursive self-referencing lattices is developed to nucleate and propagate fractures together with their stress- and scale-dependent attributes into larger domains of up to 54 m × 54 m. The advantages of this approach include preserving the nonplanarity of natural cracks, capturing the existence of long fractures, retaining the realism of variable apertures, and respecting the stress dependency of displacement-length correlations. Hydraulic behavior of multiscale growth realizations is modeled by single-phase flow simulation, where distinct permeability scaling trends are observed for different geomechanical scenarios. A transition zone is identified where flow structure shifts from extremely channeled to distributed as the network scale increases. The results of this paper have implications for upscaling network characteristics for reservoir simulation.

1. Introduction

Geomechanical modeling of the development of fracture patterns and apertures achieved on a scale spanning the laboratory specimen to perhaps a few meters is becoming relatively accurate with the latest mechanical models such as those based on the combined finite-discrete element method (FEMDEM) [*Munjiza*, 2004; *Xiang et al*., 2009; *Munjiza et al*., 2011; *Latham et al*., 2013; *Lei et al*., 2014, 2015; *Mahabadi et al*., 2014]. Many important geological phenomena can be modeled in FEMDEM numerical experiments, such as reactivation of shear on preexisting fracture walls, propagation of new cracks, and variation of aperture distribution. Due to the limits of processing power, it is currently impossible to extend this accuracy to macroscale simulation. Hence, upscaling is required to understand and evaluate important subsurface properties of large-scale naturally fractured rocks based on models established at a smaller scale.

Disordered geological media often exhibit significant scale invariance and self-similarity [*Barton and La Pointe*, 1995; *Odling*, 1997; *Berkowitz et al*., 2000; *Bour et al*., 2002]. Nontrivial power law scaling, including fractal properties, was observed in natural fracture systems [*Bonnet et al*., 2001], which often do not have a representative elementary volume (REV). An important feature of the fractal geometry and power law methods is the absence of the need for a characteristic length scale [*Bonnet et al*., 2001]. An understanding of the scaling behavior of natural fracture systems opens the possibility that hydromechanical properties of a macroscale fractured rock may be estimated based on the characterization of its crucial features from a relatively smaller sampled model [*Zimmerman and Main*, 2004].

Scaling of rock permeability has been extensively studied based on compilation of in situ measurement data [*Brace*, 1980, 1984; *Clauser*, 1992; *Neuman*, 1994; *Renshaw*, 1998]. Three measurement scales of permeability were distinguished: the laboratory scale (1–10 cm), the borehole or in situ scale (1 m–1 km), and the regional scale (1–100 km) (Figure 1) [*Clauser*, 1992]. Increase of permeability from the laboratory to the borehole scale

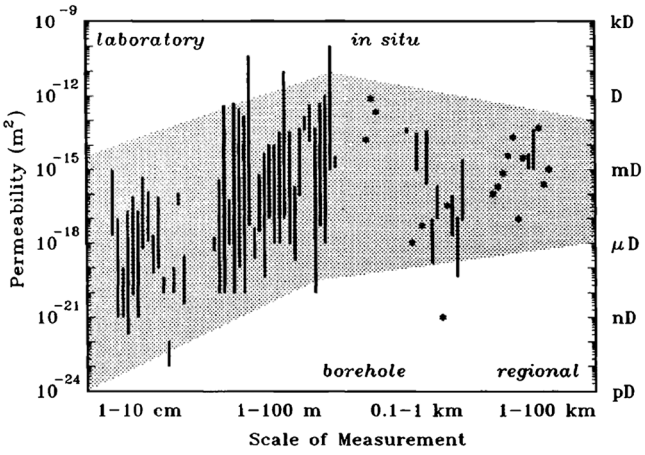

Figure 1. Permeability of crystalline rocks and characteristic scale of measurements [*Clauster*, 1992].

was observed, since laboratory tests are usually based on unfractured core specimens [*Brace*, 1980, 1984]. However, from the borehole to the regional scale, although an increasing permeability trend was reported [*Brace*, 1980, 1984; *Neuman*, 1994], so too was a plateau with no increase or a decrease [*Clauser*, 1992; *Renshaw*, 1998] (Figure 1). Rather than focusing on the broad spectrum of scales where the transition behavior depends on many complex factors (e.g., seismically visible faults, multiple rock types, and even karst features), in this paper, we choose to narrow our scope to the in situ scale (say, 1–100 m), where flow is often dominated by fractures, especially in crystalline rocks [*Clauser*, 1992], and focus on the mechanisms by which permeability of fractured rock may vary with the modeling scale over this range.

Much work using discrete fracture networks (DFNs) has focused on flow in random fractal patterns where, by neglecting geomechanical constraints, fluid transport has been modeled in networks with apertures assumed either constant [*Leung and Zimmerman*, 2012; *de Dreuzy et al*., 2001a] or statistically distributed and correlated with trace lengths [*de Dreuzy et al*., 2001b, 2002; *Klimczak et al*., 2010]. The scaling of network connectivity is dominated by the relationship between fractal dimension and power law length exponent [*Berkowitz et al*., 2000; *de Dreuzy et al*., 2001a; *Darcel et al*., 2003b], whereas the scaling of permeability is further governed by the transmissivity distribution of individual fractures [*de Dreuzy et al*., 2001b, 2002; *Davy et al*., 2006; *Klimczak et al*., 2010]. However, since geomechanically constrained apertures vary intimately with a locally varying stress field, it is an open question whether the appearance of scale invariance of network topology has useful implications for predicting effective flow properties over the ~100 m block and larger, for example, 1 km, scales.

The objective of this study is to develop a two-dimensional (2D) fracture network upscaling method to estimate hydromechanical properties of larger-scale natural fracture systems that can be based on a small-sized model. There are two distinct developments needed: (1) to construct the network topology on large domains conditioned by the data from smaller outcrops obeying a self-referencing scheme and (2) to apply geomechanical constraints to derive realistic apertures for each fracture at the outcrop scale and to propose a mechanism to preserve such aperture realism in larger scales. The paper is organized as follows. In section 2, the analogue data set is introduced together with methodologies for measuring the scaling properties of the outcrop sample in terms of spatial organization, lengths, connectivity, and displacements within the sample scale. In section 3, a network growth scheme using discrete-time random walks in a recursive self-referencing lattice is developed to grow the geologically obtained fracture pattern into larger domains with important geostatistical and geomechanical characteristics preserved, such as nonplanarity, segmentation, and aperture variability. The validity of growth networks is examined with respect to geometric properties based on a comparison between multiple growth realizations, Poissonian random networks, and an original larger analogue. Section 4 describes the method of characterizing the stress and scale dependency of fracture apertures and shear displacements as well as the principles adopted for the implementation of an indirect hydromechanical coupling. In section 5, multiscale growth networks are constructed to calculate their hydraulic properties in terms of single-phase flow tests, after which permeability scaling behavior and flow structure transition are further analyzed. Finally, a brief discussion is presented and conclusions are drawn.

2. Scaling Properties of a Natural Fracture System Within the Sample Scale

The outcrop of a natural fracture system was mapped at Kilve on the southern margin of the Bristol Channel Basin covering approximately 225 m^2 (Figure 2a) [*Belayneh et al*., 2009]. Tectonic displacement along normal

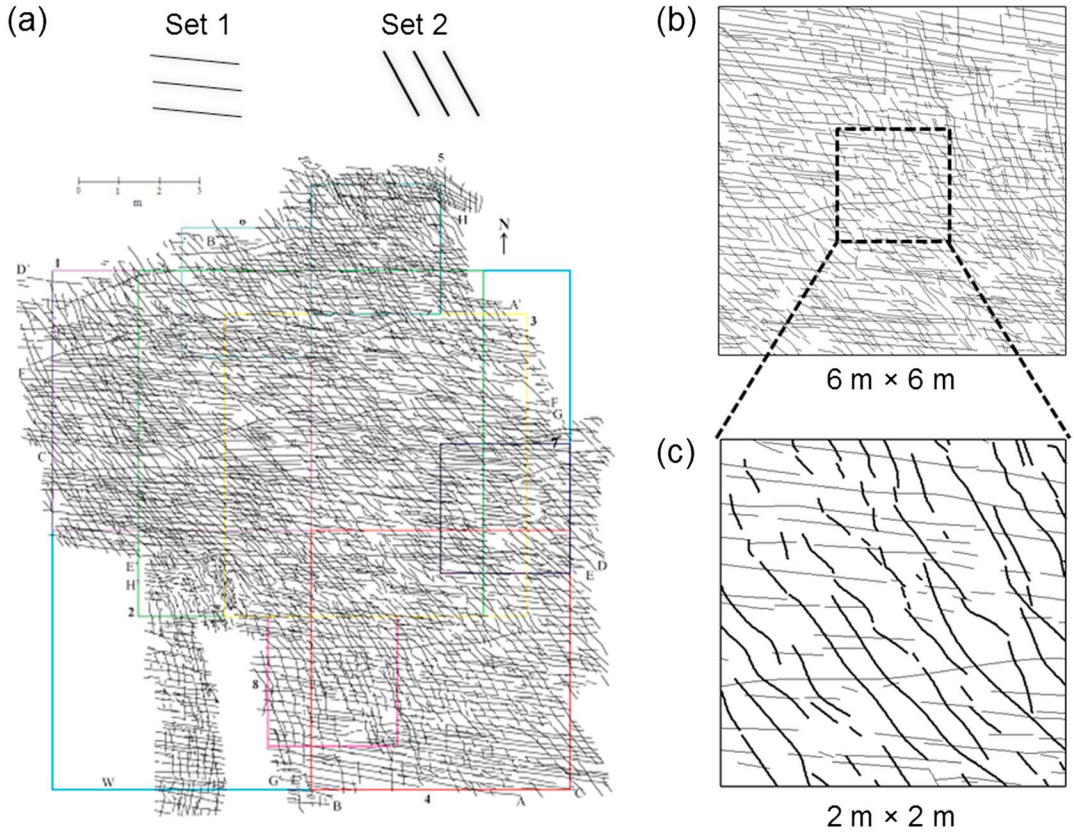

Figure 2. (a) The outcrop pattern mapped at Kilve on the southern margin of the Bristol Channel Basin [*Belayneh et al.*, 2009]. (b) Extracted 6 m × 6 m pattern for analysis of scaling properties. (c) Extracted 2 m × 2 m pattern for geomechanical modeling and as the source for network upscaling (light lines represent Set 1, and bold lines represent Set 2).

faults underlying the rift system induced porosity reduction and excess fluid pressure [*Belayneh et al.*, 2009]. During such tectonic evolution process, two oblique sets of vertical, layer-normal fractures were formed extensionally and filled with calcite minerals, striking approximately 100° (Set 1) and 140° (Set 2), respectively (note that the vein thickness will not be used for this study when deriving fracture apertures for flow prediction). The fractured limestone layer (~26 cm thick) is sandwiched between almost impervious shales, and the joint sets are layer bound [*Belayneh et al.*, 2009]. An important feature of this outcrop system is that the fracture sets are very distinct and crosscut with few abutting relationships. Two-dimensional (2D) analysis is used in this paper, while potentially important three-dimensional (3D) effects will be discussed in section 6.

The outcrop map represents a limited range of trace data of the actual fracture system controlled by the image resolution (~0.05 m) and the mapped domain size (~12 m). To eliminate the effect of irregular boundaries of the whole outcrop pattern (with unmapped areas inside the domain), a squared subarea of size $L = 6$ m containing ~1000 fractures is extracted (Figure 2b) as a sample of the fracture system to measure its scaling properties. Since it is very expensive in CPU time to compute very large domains given the current processing power [*Latham et al.*, 2013; *Lei et al.*, 2014], a smaller domain of size $L = 2$ m is selected for geomechanical modeling (section 4) and also serves as the source for network upscaling (section 5). The larger area ($L = 6$ m) will be used for checking the upscaled fracture networks generated from the source pattern ($L = 2$ m) using the proposed new approach (section 3.5).

2.1. Spatial Distribution

Fractal concepts provide a way to identify and quantify the repetition phenomenon of natural fracture systems over a wide range of scales [*Mandelbrot*, 1982]. The spatial scaling feature can be characterized by the fractal dimension D, which accounts for the manner whereby fractals cluster and spread in the

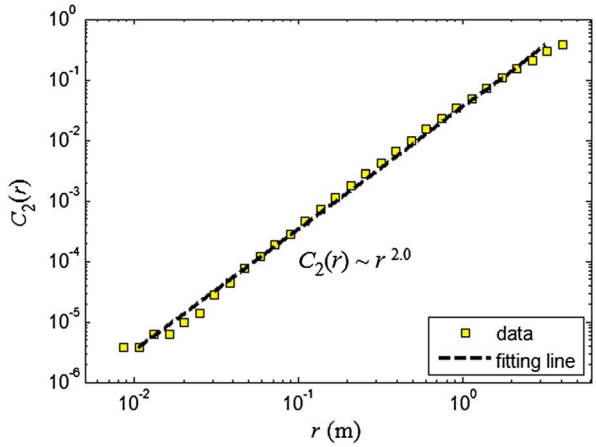

Figure 3. Calculation of the two-point correlation function $C_2(r)$ as a function of r. The slope of the least squares fitting line for data points $(r, C_2(r))$ on the bilogarithmic diagram gives an estimate of the correlation dimension $D_c \approx 2.0$.

Euclidean space. The standard or modified box-counting method has been widely used to measure the fractal dimension of complex fracture systems [*Chilès*, 1988; *Odling*, 1992; *Walsh and Watterson*, 1993; *Barton and La Pointe*, 1995; *Berkowitz and Hadad*, 1997; *Roy et al.*, 2007]. However, the box-counting method has intrinsic biases due to the presence of crossover regimes between dimensions of 1 (i.e., dimension of fracture lines) and 2 (i.e., dimension of the embedding medium) [*Odling*, 1992; *Berkowitz and Hadad*, 1997]. As a result, it is difficult to discriminate between natural fracture patterns and purely random networks, for which the two-point correlation function method can give more appropriate results [*Bonnet et al.*, 2001]. The two-point correlation function describes the spatial correlation of fracture barycenters [*Bour and Davy*, 1999] as given by

$$C_2(r) = \frac{1}{N^2} N_d(r) \sim r^{D_c} \tag{1}$$

where N is the total number of fracture barycenters and N_d is the number of pairs of barycenters whose distance is smaller than r [*Hentschel and Procaccia*, 1983]. Barycenters are calculated using the observed traces including those intersecting the boundaries, since the two-point correlation method is valid irrespective of the type of points (barycenter, fracture tips, or any random point on the fracture trace) that are used to represent fracture locations [*Bour et al.*, 2002]. For a fractal population, $C_2(r)$ is expected to scale with r following a power law relation with the exponent D_c defined as the correlation dimension. Figure 3 illustrates the scaling of $C_2(r)$ with r for the selected 6 m × 6 m pattern, where a power law trend is manifest for over two decades on the bilogarithmic diagram. By employing least squares analysis, D_c is estimated to be 2.0. Due to the fact that $D_c \leq D \leq 2.0$ (i.e., Euclidean dimension) [*Bonnet et al.*, 2001], D is also equal to 2.0, implying that the network of fracture barycenters exhibits a homogeneous filling of the 2D space and is nonfractal.

2.2. Length Distribution

A power law is often used to interpret the length distribution of natural fracture traces, and its exponent quantifies the manner that frequency decreases with fractures sizes [*Odling*, 1997; *Bonnet et al.*, 2001; *Neuman*, 2008]. The density distribution of fracture lengths (i.e., trace lengths) can be modeled by a power law [*Bour et al.*, 2002; *Davy et al.*, 2013] as given by

$$n(l, L) = \alpha L^D l^{-a} \qquad \text{for } l \in [l_{min}, l_{max}] \tag{2}$$

where $n(l, L)\mathrm{d}l$ is the number of fractures with sizes belonging to the interval $[l, l + \mathrm{d}l]$ $(\mathrm{d}l \ll l)$ in a domain of size L, α is a fracture density term, a is the power law length exponent, D is the fractal dimension, l_{min} is the minimum fracture length, and l_{max} is the maximum fracture length $(l_{min} \ll L \ll l_{max})$. The exponents a and D quantify different scaling of the fracture network: the length distribution (related to a) and the fracture density (related to D). Equation (2) is valid irrespective of D [*Bour et al.*, 2002], even for the studied nonfractal pattern. The exponent a can be derived from the cumulative distribution or density distribution of fracture lengths; however, a comparison between the two derivations of a is considered useful [*Davy*, 1993]. The observed data of fracture lengths are often biased due to the truncation (resolution limitation) and censoring effects (incomplete sampling) [*Bonnet et al.*, 2001]. A lower cutoff of 0.3 m (i.e., 5% × L) [*Odling*, 1997] is used to eliminate the truncation effect. In the cumulative distribution analysis, the censoring effect is corrected using the Kaplan-Meier method [*Odling*, 1997]. By employing least squares

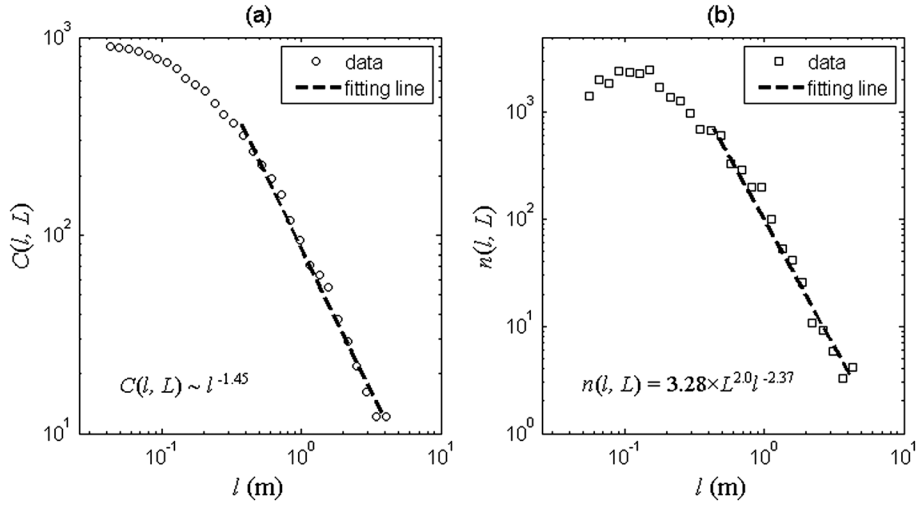

Figure 4. (a) The cumulative distribution and (b) density distribution of fracture lengths of the studied pattern having a size of $L = 6$ m. A lower cutoff of 0.3 m (i.e., $5\% \times L$) is used to eliminate the truncation effect. By correcting the censoring effect using the Kaplan-Meier method [*Odling*, 1997], the cumulative distribution gives an estimate of the length exponent $a = 1.45 + 1 = 2.45$. After removing fractures that intersect sampling boundaries and correcting the system size, the density distribution gives the length exponent $a = 2.37$ and the density term $\alpha = 3.28$.

fitting, the cumulative exponent c is estimated to be 1.45 and the length exponent is therefore calculated as $a = c + 1 = 2.45$ (Figure 4a). The cumulative distribution may suffer from an additional intrinsic bias, that is, the finite size effect [*Pickering et al.*, 1995]. In the density distribution analysis, the censoring effect is corrected by removing fractures that intersect the sampling boundaries [*Bour et al.*, 2002]. To account for the density perturbation from the artificial deletion, an effective system size is estimated as the square root of the coverage area of remaining fractures and used for the calculation of the density term α, given an assumption that the proportion of the coverage area to the squared space is equal to the ratio between the total length of remaining fractures and the total length of all sampled fractures. The length exponent a estimated from the density distribution has a slightly lower value of 2.37, and the density term α is calculated to be 3.28 (Figure 4b). The density distribution was recommended more appropriate for characterizing the length scaling behavior [*Davy*, 1993; *Bonnet et al.*, 2001] and is adopted for later analysis in this paper.

2.3. Density, Intensity, and Connectivity

If a fracture system ideally obeys the power law length distribution, its fracture density γ (i.e., number of fractures per unit area) can be derived from the integral of the density function of fracture lengths [*Darcel et al.*, 2003b], while the fracture intensity P_{21} (i.e., total length of fractures per unit area) can be derived based on the first moment of the density distribution of fracture lengths as [*Darcel et al.*, 2003b]

$$P_{21} = \frac{1}{L^2}\int_{l_{\min}}^{l_{\max}} n(l, L) l \mathrm{d}l = \frac{\alpha L^{D-2}\left(l_{\min}^{-a+2} - l_{\max}^{-a+2}\right)}{a-2} \tag{3}$$

Due to the broad range of fracture lengths, the percolation behavior of the fracture network is determined by two parts that describe the contribution from smaller and larger fractures [*Bour and Davy*, 1997] as given by

$$p(l, L) = \int_{l_{\min}}^{L} \frac{n(l, L) l^D}{L^D} \mathrm{d}l + \int_{L}^{l_{\max}} n(l, L) \mathrm{d}l \tag{4}$$

For the studied network with $a < D + 1$, if $l_{\min}$ is sufficiently small, the first integral of equation (4) is controlled by the upper bound L [*Berkowitz et al.*, 2000], which means the connectivity is only slightly dependent on $l_{\min}$. The critical system size L_c (or the connection length) corresponding to the percolation threshold can be further calculated as [*Berkowitz et al.*, 2000]

$$L_c = \left[(D + 1 - a)(a - 1)\frac{p_c}{D\alpha} + l_{\min}^{D+1-a}\frac{(a-1)}{D}\right]^{\frac{1}{D+1-a}} \tag{5}$$

for $a > 1$ and $a \neq D + 1$. The percolation threshold p_c is a scale-independent parameter with a value ranging

between 5.6 and 6.0 [*Bour and Davy*, 1997]. Here, L_c is calculated to be ~0.80 m and found marginally influenced by the given l_{min} (i.e., 0.05 m). Another feature of the scenario of $a < D+1$ is that, if the fracture density γ is fixed, the network connectivity will increase with scale; that is, the fracture network is well connected at larger scales ($L \gg L_c$) [*Davy et al.*, 2006]. For measurements based on a finite-sized domain, l_{max} is likely to be controlled by the domain size L, and consequences of such effect will be discussed in section 6.

2.4. Displacement and Length Correlation

Fractures often exhibit displacements perpendicular and/or parallel to the discontinuity surface [*Zimmerman and Main*, 2004]. They are termed aperture and shear displacement, respectively, and referred to as fracture displacement attributes in this paper.

The relation between shear displacements and fracture lengths has been extensively studied in the literature based on field measurement. By assuming a perfect positive correlation, a general form of shear displacement-length correlation law [*Bonnet et al.*, 2001] is given by

$$\delta_{max} \sim l^{n_1} \tag{6}$$

where δ_{max} is the maximum shear displacement of an individual fracture, l is the fracture length, and n_1 is the correlation exponent. A simple linear relation is predicted by the linear elastic fracture mechanics (LEFM) theory [*Pollard and Segall*, 1987]. A plane strain model taking account of inelastic deformation of faults also suggests $n_1 = 1.0$ [*Cowie and Scholz*, 1992a]. A degree of consistency has been observed between the linear scaling predictions and field measurements [*Cowie and Scholz*, 1992a, 1992b; *Dawers et al.*, 1993; *Scholz et al.*, 1993; *Kim and Sanderson*, 2005; *Schultz et al.*, 2008]. However, a range of values for n_1 have also been reported, such as 0.5 [*Fossen and Hesthammer*, 1997], 1.5 [*Gillespie et al.*, 1992], and 2.0 [*Walsh and Watterson*, 1988]. Variation of n_1 is controlled by numerous factors including lithology, growth mechanism of faults, and their interaction and reactivation [*Bonnet et al.*, 2001; *Kim and Sanderson*, 2005].

The correlation between fracture apertures and trace lengths has also been widely investigated [*Vermilye and Scholz*, 1995; *Walmann et al.*, 1996; *Renshaw and Park*, 1997; *Olson*, 2003; *Schultz et al.*, 2008]. Supposing a power correlation is also valid [*Bonnet et al.*, 2001], apertures can then be related to fracture lengths as

$$b_{max} \sim l^{n_2} \tag{7}$$

where b_{max} is the maximum aperture of an individual fracture, l is the fracture length, and n_2 is the correlation exponent. The exponent n_2 was proposed to range between 0.5 and 2.0 [*Bonnet et al.*, 2001; *Neuman*, 2008]. A square root sublinear scaling law was derived by incorporating subcritical and critical fracture propagation criteria into LEFM analysis [*Olson*, 2003] and is given by

$$b_{max} = \frac{K_{Ic}(1-\upsilon^2)}{E\sqrt{\pi/8}} l^{0.5} \tag{8}$$

where K_{Ic} is the mode I fracture toughness, E is Young's modulus, and υ is Poisson's ratio. For plane strain conditions, K_{Ic} is related to the energy release rate G by

$$G = K_{Ic}^2 \left(\frac{1-\upsilon^2}{E}\right) \tag{9}$$

By assuming fracture opening shape to be elliptical in nature, the average aperture b_{avg} can be related to b_{max} [*Olson*, 2003] as

$$b_{avg} = \frac{\pi}{4} b_{max} = \sqrt{\frac{\pi G(1-\upsilon^2)}{2E}} l^{0.5} \tag{10}$$

The square root model shows good agreement with field observations [*Walmann et al.*, 1996; *Olson*, 2003; *Schultz et al.*, 2008; *Klimczak et al.*, 2010]. However, variation of n_2 still exists due to the interaction among fractures in the actual geological environment [*Hatton et al.*, 1994; *Vermilye and Scholz*, 1995; *Renshaw and Park*, 1997].

In reality, the scaling exponents (i.e., n_1 and n_2) are not only determined by topological attributes but also governed by geomechanical constraints, for example, the magnitude and orientation of in situ stresses. In

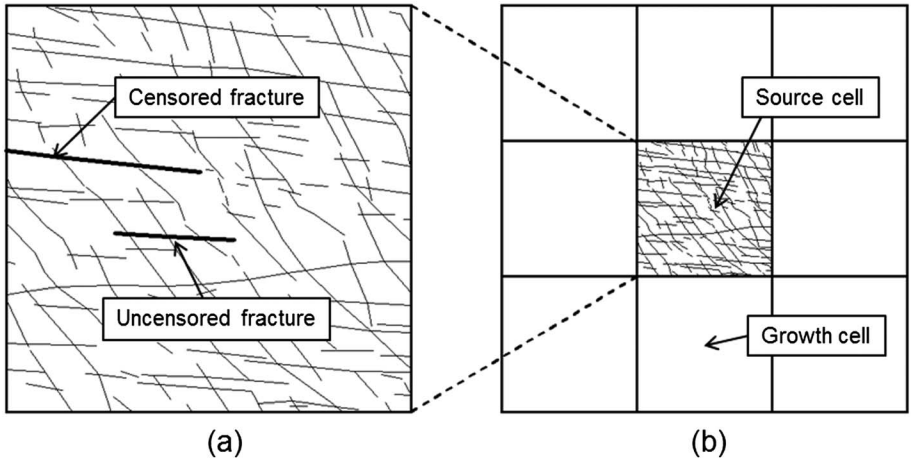

Figure 5. (a) The source cell pattern involving censored and uncensored fractures and (b) a growth lattice consisting of one source cell and eight growth cells.

this research, the scaling exponents will be derived based on geomechanical modeling of a fractured rock under in situ stress conditions. For simplicity, fractures are associated with no initial phase of shearing, whereas initial apertures are assigned a priori using equation (10) to model rupture-induced initial opening. A further application of assumed far-field stresses using the FEMDEM geomechanical model will illustrate the accommodation of closure, opening, shearing, and dilatancy in the fracture system and introduce variability to the distribution of displacement attributes (section 4.1). The resulting stress-dependent distribution is to be preserved in a scaled and coupled way during the formation of growth networks (sections 4.2 and 4.3).

3. Fracture Network Growth Model

3.1. Growth Lattice

By assuming the fracture system fills progressively larger and larger Euclidean space domains in a repeatable process, a novel scheme is developed to grow the geologically obtained fracture pattern together with its spatially variable displacement attributes (i.e., fracture aperture and shear displacement) into larger scales using a growth lattice (Figure 5b). There are two types of cells in a growth lattice: the source cell (SC) that is the reference for network growth and the growth cell (GC) that is a clone of the SC sharing common geostatistics. Here the source cell corresponds to the $2\,\mathrm{m} \times 2\,\mathrm{m}$ outcrop sample. Important characteristics of the source network will be retained during a growth process: (i) at the population level, fracture density and spatial distribution are matched by GCs to the SC; (ii) at the individual fracture level, various properties including orientation, length, segmentation, curvature, and displacements are preserved. The fractures are classified into censored (partially sampled) and uncensored (completely observed) types (Figure 5a), each of which requires distinct means for extrapolation. Boundary constraints are applied along the cell periphery to guarantee topological connectivity. The growth procedure is implemented separately for each set due to the intrinsic difference in their geostatistical properties.

3.2. Source Cell Geostatistics

Methods of geostatistics are applied to the source pattern to interpret its topological complexity in a quantitative way. Location of censored fractures is measured based on the distribution of censoring nodes, through which partially sampled fractures are truncated by the SC boundary. Spatial organization of uncensored fractures is delineated by the distribution of their barycenters, based on a physically reasonable assumption that barycenter is likely to be the initial nucleus position for idealized symmetrical crack development [*Bour et al.*, 2002]. Two exclusion parameters, that is, exclusion radius and spacing, are computed for each barycenter based on its spatial relationship with other nuclei (Figure 6). The exclusion radius of a barycenter is the distance with the closest counterpart, while the exclusion spacing is measured by projecting the point cloud to a line perpendicular to the mean

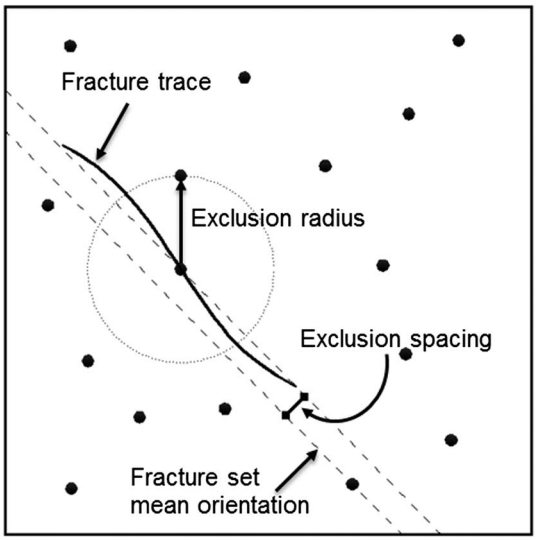

Figure 6. Barycenter map for characterizing fracture exclusion radius and spacing.

orientation of the fracture set. The procedure allows the preservation of fracture barycenter spatial distribution. The SC spatial information is synthesized into a mathematical expression given by

$$X_i = \chi(\varepsilon_n, \varepsilon_r, \varepsilon_s) \tag{11}$$

where X_i corresponds to the location of the barycenter of the ith source fracture and ε_n, ε_r, and ε_s denote the probability density functions (PDFs) for the distribution of spacing of censoring nodes, exclusion radius, and spacing of barycenters, respectively, determined from a series of nonparametric Kolmogorov-Smirnov hypothesis tests.

Characteristics of individual fractures are also statistically quantified for various key respects. The property, priority degree, is measured for each fracture based on the ratio of its length to the size of the SC domain. For example, a censored fracture with a ratio greater than 1.0 is potentially a traversing fracture in larger scales and is associated with a high priority. The number of segments of each source fracture is counted and will be used later to determine the duration of the discrete-time sequence for each random walker, discussed in section 3.3.1. Curvature of multisegment fracture traces is governed by the inflection nature as well as orientation dispersion (Figure 7). It is a property that can greatly influence the tortuosity of migration path for subsurface flow [*Ronayne and Gorelick*, 2006] (a simple demonstration is given in Appendix A). The number of inflection points, $\tilde{n}$, is counted for each naturally bent fracture by identifying the concavity sign transition based on the second derivatives of the nonuniform rational basis spline (NURBS) in the 2D Cartesian coordinate system. Hypothesis tests are conducted to choose an optimal distribution (e.g., uniform, normal, lognormal, exponential, or gamma) for segmental lengths, orientations, shear displacements, and apertures with their truncated PDFs denoted as $g_i(l)$, $h_i(\theta)$, $u_i(\delta)$, and $v_i(b)$, respectively, for the ith source fracture. For development of $u_i(\delta)$ and $v_i(b)$, see section 4.1. The segmental statistical properties are measured independently for each source cell fracture to account for their nontrivial length dependency and intercorrelation. For example, a longer fracture is prone to be more bent (see Figure 2c) and have greater trajectory variation, that is, greater dispersion in segmental orientation, for the reason that it occupies a larger space and the growth path can be more influenced by stress heterogeneity and other existing fractures. Furthermore, the aperture and shear displacement may be greatly affected by the degree of curvature.

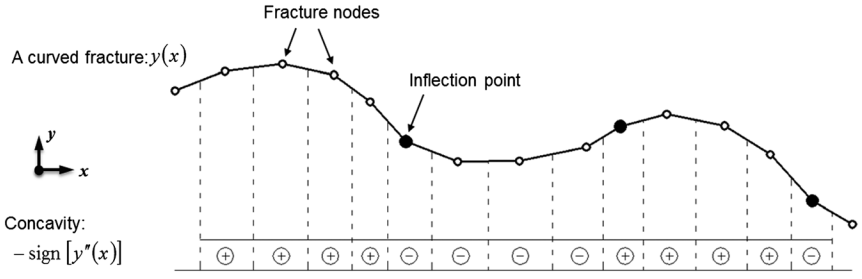

Figure 7. Characterization of the curvature of a multisegment fracture NURBS based on the transition between concavity and convexity.

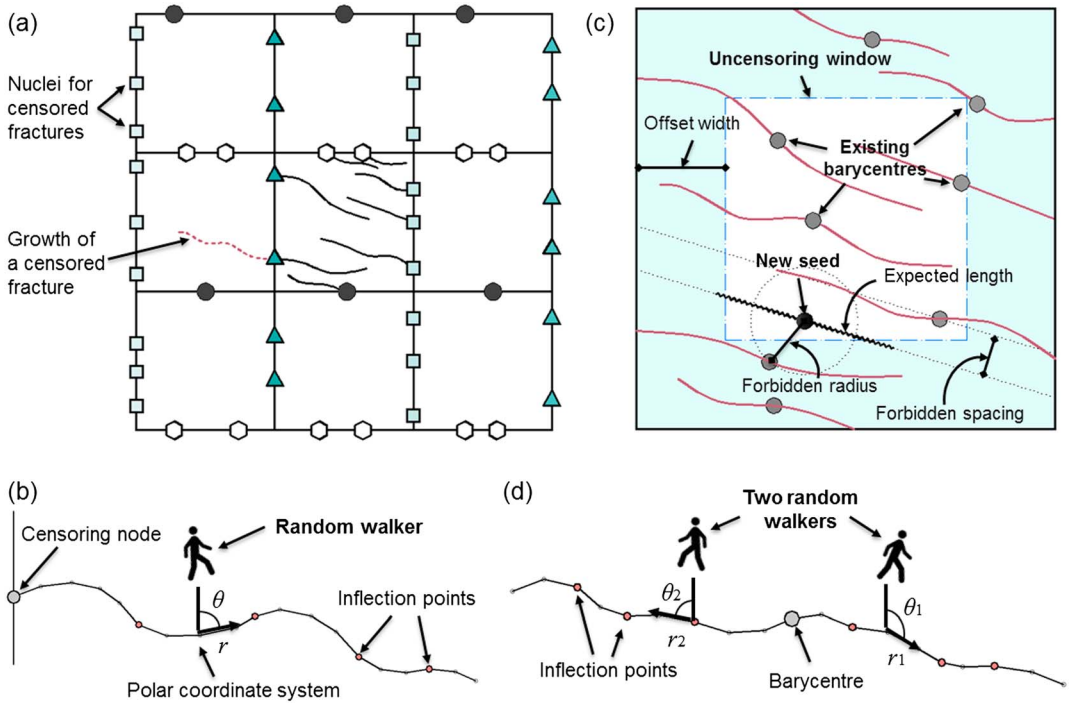

Figure 8. (a) Nucleation of censored fractures by seeding censoring nodes along edges of the growth lattice, (b) propagation of a censored fracture from a censoring node simulated by a random walker, (c) nucleation of uncensored fractures by a point packing process constrained by the barycenter exclusion parameters, and (d) propagation of an uncensored fracture from its barycenter captured by two synchronized random walkers.

3.3. Growth of Fractures

3.3.1. Growth Formulation

The nucleation process of fractures in GCs, according to the self-referencing scheme, is governed by the spatial information model of the source sample as

$$X_i^0 = \chi(\varepsilon_n, \varepsilon_r, \varepsilon_s) \tag{12}$$

where X_i^0 is the position of a random nucleus for the ith growth fracture. Propagation of fractures from nuclei is simulated through discrete-time random walks in a polar coordinate system [*Kaye*, 1994], in which a fracture is traced by variable jumps from one position to another as time proceeds:

$$X_i^{t+1} = X_i^t + \Delta X_i^t \tag{13}$$

where $t \in \{0, 1, 2\ldots, T_i\}$ is the discrete time in sequence, T_i corresponds to the prospective number of segments of the ith growth fracture, X_i^t is the position of the walker at the time t, and ΔX_i^t is the increment for the next step governed by a multivariate distribution given by

$$f_i(\Delta X_i^t) = g_i(l)h_i(\theta|\lambda^t\theta^t \geq \lambda^t\theta^{t-1}) \tag{14}$$

where l and θ are two independent random variables for segmental length and orientation, respectively, which are generated in a bootstrapping process based on the corresponding source fracture statistics, and λ^t is a sign variable indicating the current concavity state that switches from plus to minus or vice versa if the walker passes an inflection point that is associated to the discrete-time sequence through a Bernoulli process with a success probability of $\tilde{n}/(T+1)$. Amplitude of a curved trace is modeled by a conditional distribution, that is, the second part of the right-hand side of equation (14), so that the orientation variable monotonically increases or decreases in each period between inflection nodes, with the degree of curvature controlled by the standard deviation. Fracture displacement variables, that is, δ and b, are stochastically generated using the probability functions $u_i(\delta)$ and $v_i(b)$ and automatically assigned to each segment as walkers parade.

In the numerical implementation, the growth of censored and uncensored fractures in GCs is achieved in different ways due to their distinct sampling features. Nuclei of censored fractures are seeded along lattice

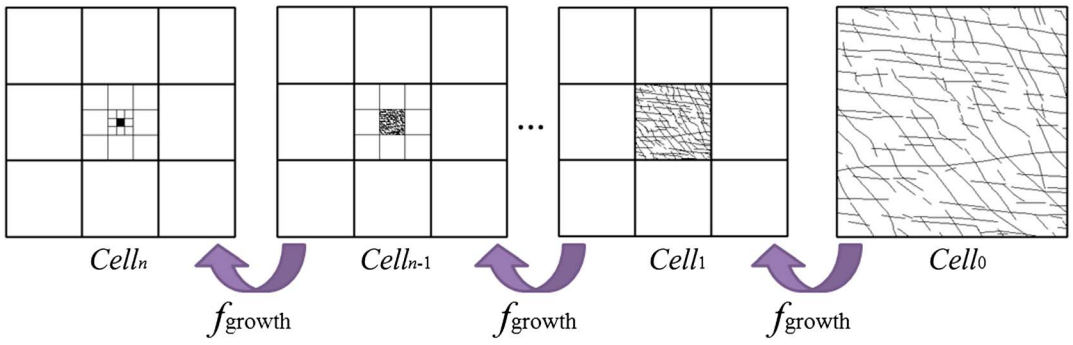

Figure 9. Recursive cell culture scheme.

edges, while barycenters of uncensored fractures are spawned inside cell domains. In each growth region, censored fractures are grown ahead of uncensored ones and will place constraints for barycenter nucleation. The mechanism of geological arresting [*Davy et al.*, 2013] is not included in this growth scheme on account of the crosscutting feature of the source pattern, which means that each random walk is an independent process.

3.3.2. Growth of Censored Fractures

Following the self-referencing scheme, GCs are prescribed to share a similar window-censoring condition to the SC due to the same occupation area in the 2D Euclidean space. Censoring nodes are randomly seeded along lattice edges, except those belonging to the central SC (Figure 8a). Adjacent cells are constrained to have the same nodes along their identical edge to guarantee the connectivity between them, while their nonoverlapped edges are equipped with statistically mirrored settings. A censored growth fracture in GCs evolves from a nucleus located on the lattice edge with its propagation traced by a random walker (Figure 8b). The censoring nodes already connected with fractures from neighbor cells are hatched first, and new fractures are forced to propagate with the priority degree retained. Other isolated censoring nodes are arbitrarily allocated with the remaining fracture statistics from SC data sets. Censored fractures are grown first in the four GCs neighboring the SC, which can place priority constraints for the nuclei along the edges shared with other GCs located at lattice corners.

3.3.3. Growth of Uncensored Fractures

Nucleation of uncensored fractures is modeled by a point packing process (Figure 8c). Barycenters of already generated censored fractures are identified to draw an initial barycenter map. An uncensoring window offsetting a width from the cell periphery is recognized to be the domain for coordinate generation, where an uncensored fracture has little chance to touch cell borders. The offset width is calculated based on the expected values of the length and orientation of the current propagating fracture. Inserting a new nucleus into the barycenter cloud is constrained by the frequency distribution of exclusion parameters. The distance between a new seed and the closest existing barycenter cannot be smaller than a random variable of the exclusion radius, while the minimum spacing with existing fractures also has to be larger than a stochastic value of exclusion spacing. If the new seed does not satisfy these criteria, it will be abandoned and another candidate will be generated. This process is repeated under an automated mechanism until the candidate can pass the examination, after which the map will be updated with the new nucleus added. An uncensored crack hatches from the barycenter nucleus and propagates as two synchronized walkers jogging toward opposite directions (Figure 8d).

3.4. Recursive Cell Culture

A recursive cell culture scheme is implemented to extrapolate fracture networks into larger lattices under a self-referencing scheme (Figure 9). The recursive formulation is given by

$$\begin{cases} \text{Cell}_n = f_{\text{growth}}(\text{Cell}_{n-1}) \\ \text{Cell}_0 = \text{initial SC} \end{cases} \tag{15}$$

where the nth-order cell is grown from the $n-1$th-order cell which serves as the source cell in the nth phase, f_{growth} is the growth function based on random walks in the nine-grid lattice, and the zeroth-order cell corresponds to the initial SC. In each growth phase, censored fractures from different cells are connected, followed by the establishment of a new SC geostatistical library based on the larger network for next phase cell culture.

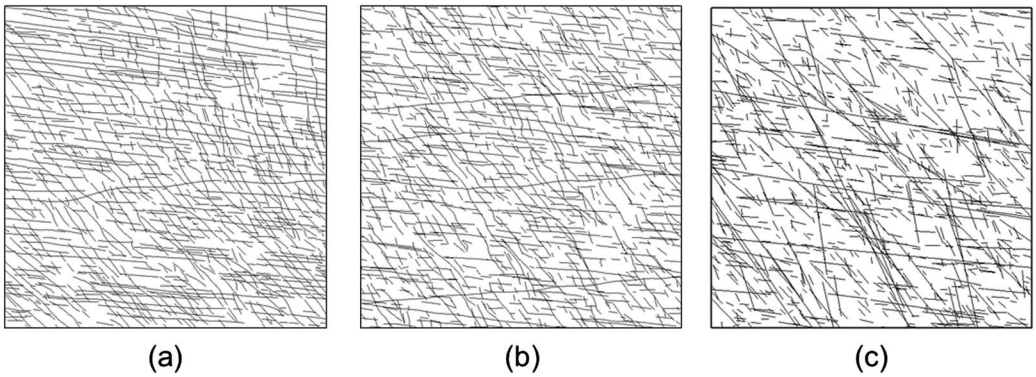

Figure 10. Fracture patterns (domain size $L = 6$ m) of (a) the analogue fracture network (AFN), (b) one of the 10 growth fracture network (GFN) realizations, and (c) one of the 10 Poissonian discrete fracture network (DFN) realizations.

3.5. Validity of Growth Networks

To examine the validity of growth networks for representing larger fracture systems, a comparison is made at a system scale of $L = 6$ m between the original analogue fracture network (AFN) from outcrop mapping (Figure 10a), 10 realizations of growth fracture network (GFN) cultivated from the central $L = 2$ m source pattern (Figure 10b), and 10 realizations of pure Poissonian discrete fracture network (DFN) (Figure 10c). A Poissonian DFN is created by the following steps: (1) generating fracture barycenters using a Poisson process with the barycenter density equal to that of the AFN, (2) sampling random lengths conditioned by the power law statistics obtained in section 2, (3) assigning fracture orientations (uncorrelated with lengths) using a bootstrapping process from the orientation data of the AFN, and (4) deleting the fracture portions that are outside the domain. Observation of Figure 10 highlights some interesting differences in visual appearances. The AFN and GFN appear subtly different, since the central $L = 2$ m source cell does not fully feature the characteristics of the original AFN, such as the relatively long and straight Set 1 fractures as can be seen in the top left region of Figure 10a as well as the significant swing in the orientation of Set 2 from the lower left to top right corner. However, the much disordered appearance of Figure 10c is in stark contrast to the other two, possibly due to the uncorrelation between lengths and orientations in the DFN system [*Odling*, 1992]. A quantitative comparison is further given as shown in Table 1.

In Table 1, fractal dimension D is derived from the two-point correlation function, length exponent a is estimated from the density distribution of fracture lengths, fracture intensity P_{21} is calculated using equation (3), and percolation parameter p is computed from equation (4). Intersection density ω is measured as the number of intersection nodes per unit area. It can be noted that the GFN realizations show quite similar results to the AFN, although certain discrepancy still exists. The AFN has a slightly higher P_{21} value than GFNs possibly caused by intrinsic heterogeneity of geological media and potential scale dependency of P_{21} (a further discussion is given in section 6). The GFNs have a fractal dimension approximately equal to 2, indicating that the nonfractality of the barycenter spatial distribution is preserved. Larger length exponent (i.e., fewer long fractures) in the GFNs is probably a result of the sampling bias of the limited source data as already observed in the visual comparison. However, the Poissonian DFNs seem to underestimate several important properties, for example, P_{21} and ω, despite there being a quite good match with respect to a and p. Figure 11 further compares the spacing distribution of the three types of networks measured by placing 20 scanlines along the north-to-south

Table 1. Comparison Between the Analogue Fracture Network (AFN), Growth Fracture Networks (GFNs), and Poissonian Discrete Fracture Networks (DFNs) With the Domain Size $L = 6$ m

Properties	AFN	GFNs	DFNs
Fractal dimension D	2.00	1.96 ± 0.04	1.92 ± 0.06
Length exponent a	2.37	2.54 ± 0.05	2.42 ± 0.13
Fracture intensity P_{21} (m^{-1})	11.23	10.67 ± 0.04	9.26 ± 0.37
Percolation parameter p	12.14	11.55 ± 0.26	13.44 ± 1.33
Intersection density ω (m^{-2})	23.81	23.79 ± 0.64	18.47 ± 6.33

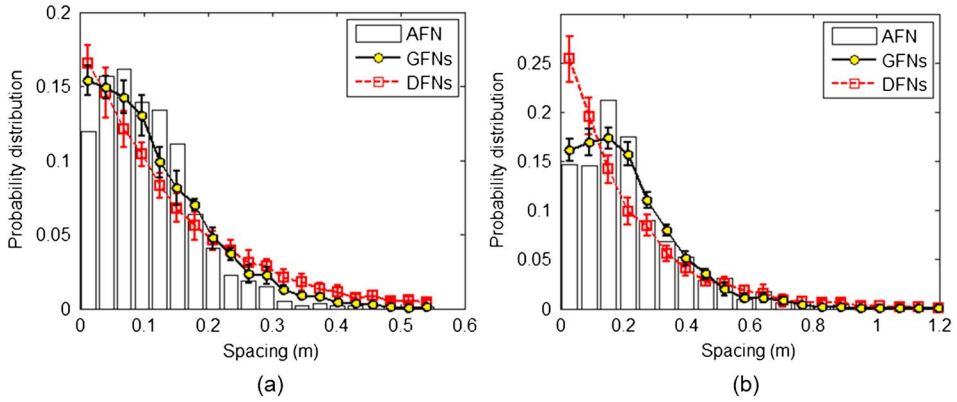

Figure 11. Spacing distribution of the AFN, GFNs, and DFNs measured by placing 20 scanlines along (a) the north-to-south direction and (b) the east-to-west direction, respectively, for each fracture pattern.

direction and the east-to-west direction, respectively, for each pattern. It seems that the AFN exhibits a "lognormal-like" spacing distribution, while the DFNs tend to have an "exponential-like" distribution since there is no constraint for very close barycenters in the Poisson process. The growth model tends to present a more realistic spacing distribution under the control of the exclusion parameters, although certain discrepancies still exist probably in relation to the bias in predicting the length distribution. Generally, the growth patterns exhibit quite a good match to the actual fracture system regarding geometric properties.

4. Characterization of Fracture Attributes

Fracture attributes, that is, aperture and shear displacement, of hierarchical rock structures exhibit significant stress dependency [*Min et al*., 2004; *Baghbanan and Jing*, 2008; *Latham et al*., 2013; *Lei et al*., 2014, 2015] and scale dependency [*Hatton et al*., 1994; *Walmann et al*., 1996; *Renshaw and Park*, 1997; *Bonnet et al*., 2001; *Kim and Sanderson*, 2005; *Neuman*, 2008]. Geomechanical modeling is conducted on the 2 m × 2 m rock sample to obtain a realistic distribution of fracture attributes, which will be transformed into larger networks following proper scaling laws. Solid-to-fluid coupling is modeled under an indirect mechanism [*Rutqvist and Stephansson*, 2003] representing the change in hydraulic parameters caused by applied in situ stresses to solid skeletons [*Min et al*., 2004; *Baghbanan and Jing*, 2008; *Paluszny and Matthäi*, 2010; *Latham et al*., 2013; *Lei et al*., 2014, 2015].

4.1. Stress Dependency of Fracture Attributes

A plane strain numerical experiment is designed with biaxial effective stresses applied by different ratios, that is, a hydrostatic stress case with $\sigma_x'/\sigma_y' = 1$ and a deviatoric stress case with $\sigma_x'/\sigma_y' = 2$, given that $\sigma_y' = 5$ MPa. Material properties of limestones vary widely, and those of a type of limestone deemed to be typical [*Lama and Vutukuri*, 1978] are chosen as given in Table 2. To eliminate artificial shock, far-field stresses are applied at the model boundaries by a ramping stage from an unstressed state, and the fractured limestone adjusts to a new deformed state under the two different stress scenarios considered. Stress effect on the variability of fracture attributes is characterized in two respects [*Lei et al*., 2014, 2015]: (1) opening and shearing caused by network-scale fracture and matrix interaction under applied far-field stresses (referred to here as mesoscopic effect) and (2) closure and dilation

Table 2. Material Properties of a Typical Type of Limestone

Properties	Value	Unit
Density	2700	kg m^{-3}
Young's modulus	30	GPa
Poisson's ratio	0.27	--
Joint friction coefficient	0.6	--
Internal friction coefficient	1.0	--
Rock tensile strength	7.0	MPa
Rock cohesion	15	MPa
Energy release rate	1	kJ m^{-2}
JCS	100	MPa
JRC	5	--

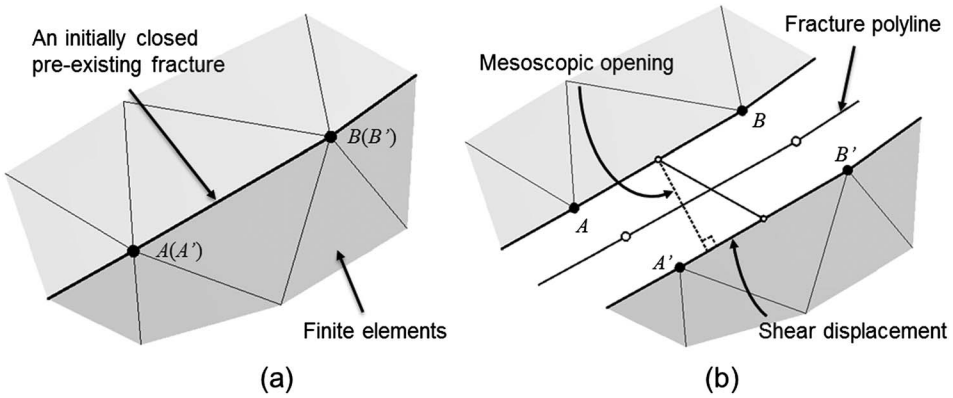

Figure 12. Representation of a preexisting fracture in (a) the initial closed state and (b) a deformed state after opening and sliding [*Lei et al.*, 2014].

governed by fracture-scale roughness under local compressive stress and shearing movement (referred to as microscopic effect).

Network-scale fracture behavior is modeled by the combined finite-discrete element method (FEMDEM) [*Munjiza*, 2004; *Xiang et al.*, 2009; *Munjiza et al.*, 2011], which is capable of simulating the deformation and stress heterogeneity of a rock matrix, reactivation and interaction of preexisting fractures, and propagation of new cracks caused by mode I or mode II brittle failure [*Latham et al.*, 2013; *Lei et al.*, 2014]. An unstructured grid is created with fracture walls represented by the opposite finite element edges, whose nodes are initially set to share identical coordinates (Figure 12a). Fracture opening b_{meso} and shear displacement δ_s induced by the mesoscopic effect are calculated explicitly as the normal and tangential components of nodal distance of edge pairs along deformed fracture walls (Figure 12b) [*Lei et al.*, 2014].

Normal deformation of a fracture with two facing walls being in contact under the local compressive stress is governed by the microscopic roughness effect, which is modeled implicitly by a nonlinear hyperbolic function [*Bandis et al.*, 1983] given as

$$b_{\text{micro}} = b_0 - \frac{1}{\frac{1}{v_m} + \frac{K_{ni}}{\sigma_n'}} \tag{16}$$

where b_{micro} is the current aperture (mm), b_0 is the a priori initial aperture (mm) correlated with fracture length according to equation (10), K_{ni} is the initial normal stiffness (MPa/mm), v_m is the maximum allowable closure (mm), and σ_n' is the effective normal stress (MPa). The parameters K_{ni} and v_m can be estimated using joint roughness coefficient (JRC) and joint compressive strength (JCS) [*Bandis et al.*, 1983] as

$$K_{ni} = -7.15 + 1.75\ \text{JRC} + 0.02 \times \frac{\text{JCS}}{b_0} \tag{17}$$

$$v_m = -0.1032 - 0.0074\ \text{JRC} + 1.1350 \times \left(\frac{\text{JCS}}{b_0}\right)^{-0.2510} \tag{18}$$

Coefficients derived based on experimental measurements of 64 joint samples of five different rock types under a third loading cycle are adopted because in situ fractures are considered more likely to behave in a manner similar to the third or fourth cycle [*Barton et al.*, 1985]. These empirical equations and coefficients can statistically interpret the observed behavior of the experiment samples under the specific testing conditions [*Bandis et al.*, 1983]. However, attention is needed if they are applied to actual engineering and geological problems [*Baghbanan and Jing*, 2008]. It can be noted that K_{ni} and v_m are both length dependent due to the a priori length correlation of the initial aperture b_0. A longer fracture associated with a larger initial aperture has a smaller normal stiffness and a larger allowable closure. The heterogeneous stress field captured at the network scale by the FEMDEM model is loaded piecewisely on local fracture walls to compute the closure of local apertures. The normal aperture b_n is calculated by combining the mesoscopic and microscopic effects as given by

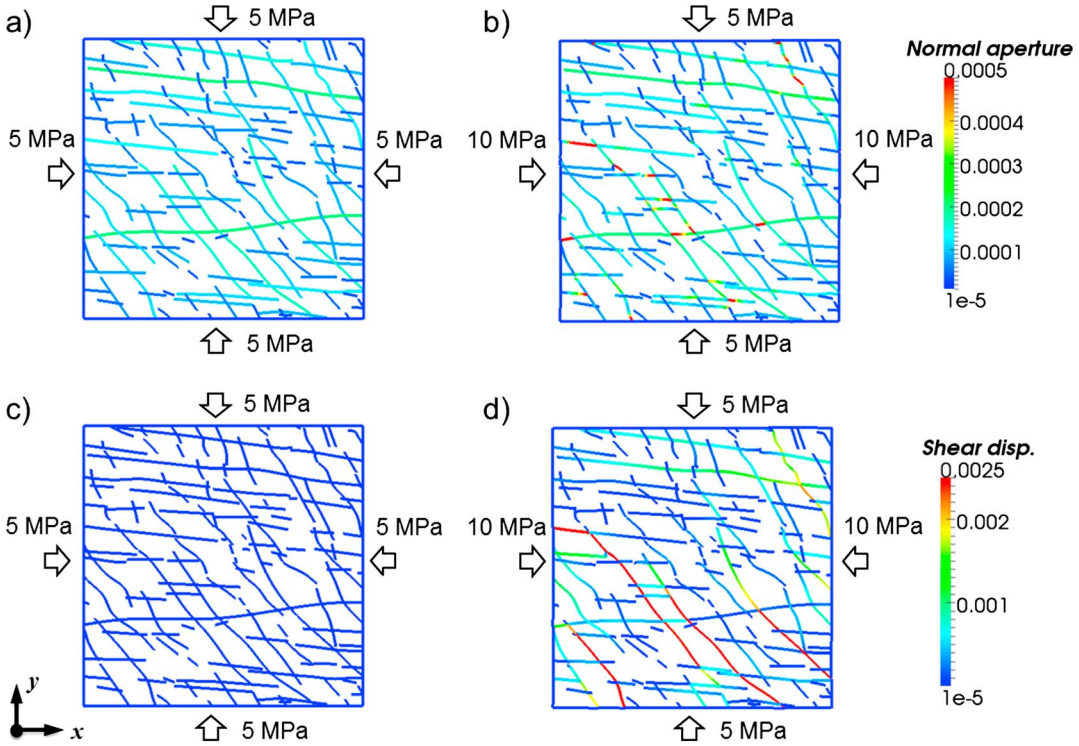

Figure 13. Aperture distribution of the fractured rock in response to different biaxial stress conditions: (a) a hydrostatic case with $\sigma_x^{'} = 5$ MPa and $\sigma_y^{'} = 5$ MPa and (b) a deviatoric case with $\sigma_x^{'} = 10$ MPa and $\sigma_y^{'} = 5$ MPa. Shear displacement distribution of the fractured rock in (c) the hydrostatic case and (d) the deviatoric case.

$$b_n = \begin{cases} b_{meso} + b_0, & \text{if } b_{meso} > 0 \\ b_{micro}, & \text{if } b_{meso} \le 0 \end{cases} \tag{19}$$

The aperture model presented here can capture the scenario where the two facing fracture walls are either open ($b_{meso} > 0$) or in contact ($b_{meso} \le 0$).

As shown in Figure 13a, longer fractures exhibit relatively larger apertures under the hydrostatic condition, mainly controlled by the a priori correlation with fracture lengths. However, variation is observed in the deviatoric case (Figure 13b), where some quite large apertures emerge locally caused by dilational bends in curved fractures, dilational jogs at sheared intersections, and fracture openings along rotated block boundaries [*Latham et al.*, 2013]. The influence of in situ stress ratio on shear displacement distribution is more remarkable. In the hydrostatic case, all fractures are suppressed for shearing (Figure 13c), whereas significant sliding occurs in the deviatoric condition (Figure 13d), especially associated with Set 1 due to its favorable orientation.

4.2. Scale Dependency of Fracture Attributes

Scaling exponents, that is, n_1 and n_2, of fracture attributes can be derived by statistical correlation analysis and are found greatly influenced by the in situ stress state. As shown in Figure 14a, fracture apertures in the hydrostatic case experienced significant closure from their initial values. However, deformed apertures still tend to follow a power law relation with fracture lengths, believed to be mainly caused by the a priori square root correlation. The nonlinear relation between aperture closure and fracture length (as seen by combining equations (16)–(18)) adjusted the exponent n_2 to be 0.568 in the hydrostatic condition. Geomechanically induced variability under deviatoric stresses is well captured, and a higher exponent is obtained, that is, $n_2 = 0.635$. The higher exponent can be possibly attributed to the tendency that a longer fracture may generate more openings due to more locally curving parts of the fractures (where it is easier to form dilational bends) and more intersections with other fractures (where it is easier to accommodate dilational jogs). Shear displacements also show a power law trend with scale (Figure 14b). Fractures under

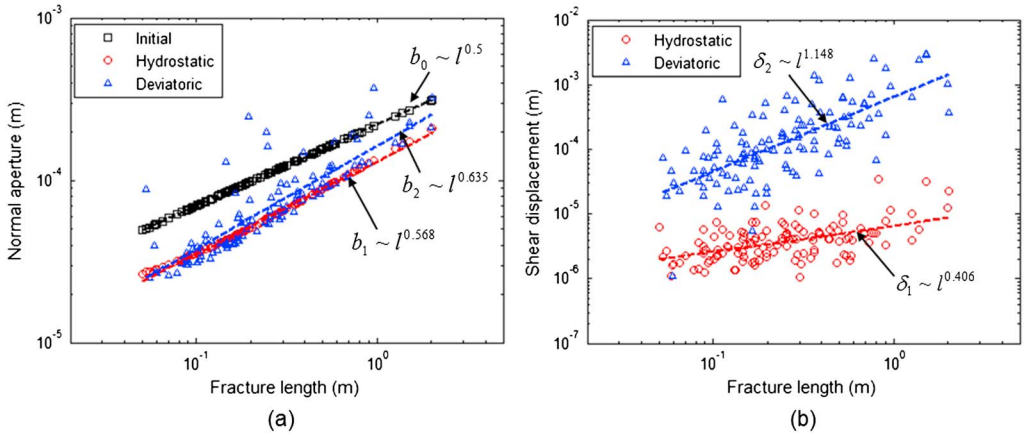

Figure 14. (a) Correlation between length-weighted average apertures and fracture lengths and (b) correlation between length-weighted average shear displacements and fracture lengths of the 2 m × 2 m fractured rock under different in situ stress conditions.

the deviatoric condition are associated with a much higher exponent ($n_1 = 1.148$) than those under the hydrostatic condition ($n_1 = 0.406$). Such aperture and shear displacement scale dependencies produced by the geomechanical model are considered important and realistic for these unique scenarios.

During the formation of growth networks, when fractures are connected with each other via cell boundaries to form a longer fracture, their displacement attributes will be upgraded by multiplying a scaling factor ζ deduced from equations (6) and (7):

$$\zeta = \frac{l_l^n}{l_s^n} = \left(\frac{l_l}{l_s}\right)^n \tag{20}$$

where l_s is the length of a shorter fracture which will connect with other shorter fractures to form a longer one with length l_l and n is the scaling exponent to be substituted by n_1 or n_2 for shear displacement or aperture, respectively. The upgrading operation is implemented automatically in each growth phase.

4.3. Coupling of Fracture Attributes With a Fracture Dilation Model

For each growth network, its scaled aperture and shear displacement can be mechanically coupled according to a fracture dilation model [*Asadollahi and Tonon*, 2010] to account for shear-induced dilational displacement b_s given by

$$b_s = \begin{cases} \frac{1}{3}\delta_s\left(\frac{2\delta_s}{\delta_{peak}} - 1\right)\tan\left[\mathrm{JRClog}_{10}\left(\frac{\mathrm{JCS}}{\sigma_n'}\right)\right], & \delta_s \le \delta_{peak} \\ \int_{\delta_{peak}}^{\delta_s} \tan\left[\mathrm{JRClog}_{10}\left(\frac{\mathrm{JCS}}{\sigma_n'}\right)\left(\frac{\delta_{peak}}{\delta}\right)^{0.381}\right] d\delta + b_{s,peak}, & \delta_s > \delta_{peak} \end{cases} \tag{21}$$

where δ_s is the fracture shear displacement, δ_{peak} is the peak shear displacement, $b_{s,peak}$ is the dilational value at δ_{peak}, and σ_n' is the effective normal stress applied on fracture walls. Peak shear displacement is a stress- and scale-dependent parameter that can be estimated using an empirical relation [*Asadollahi and Tonon*, 2010]:

$$\delta_{peak} = 0.0077 \times l^{0.45}\left(\frac{\sigma_n'}{\mathrm{JCS}}\right)^{0.34}\cos\left(\mathrm{JRClog}_{10}\left(\frac{\mathrm{JCS}}{\sigma_n'}\right)\right) \tag{22}$$

where l is the effective joint length (or block size) [*Barton*, 1981] calculated as the average spacing of cross-joints. Normal stress σ_n' is estimated using the Mohr circle equation:

$$\sigma_n' = \frac{1}{2}\left(\sigma_x' + \sigma_y'\right) + \frac{1}{2}\left(\sigma_x' - \sigma_y'\right)\cos 2\theta + \tau_{xy}'\sin 2\theta \tag{23}$$

where σ_x' and σ_y' are the values substituted from the applied far-field stresses, τ_{xy}' is equal to 0, and θ is the intersection angle between the normal of the fracture plane and the positive x direction. The integral part

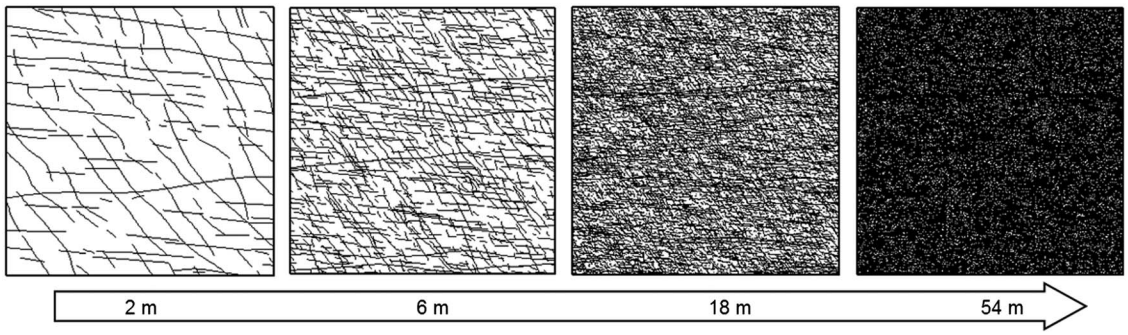

Figure 15. Multiscale growth realizations achieved by the recursive cell culture scheme.

in equation (21) is numerically approximated by the quadratic solution of the three-point Simpson rule. In the hydrostatic case, not surprisingly, the dilational effect scarcely exists since $\delta_s \ll \delta_{peak}$.

Mechanical aperture b_m is derived as the summation of the dilational displacement and the scaled normal aperture. Hydraulic aperture b_h, defined as an equivalent aperture for laminar flow between smooth parallel plates, may exhibit a complicated nonlinear correlation with mechanical aperture [*Barton et al.*, 1985; *Olsson and Barton*, 2001]. For simplicity, hydraulic aperture in this research is treated equally to mechanical aperture, which tends to overestimate flow rates by a roughness-dependent factor of ≤ 2 [*Matthäi and Belayneh*, 2004]. However, this bias is considered not to have a significant influence for the focus of the study in this paper, which is the trend by which permeability is likely to change over length scales.

5. Multiscale Growth Networks With Stress- and Scale-Dependent Apertures

5.1. Multiscale Growth Network Realizations

Multiscale growth networks with stress- and scale-dependent apertures are constructed through the recursive cell culture scheme based on the stressed 2 m × 2 m Kilve analogue sample. Figure 15 presents one realization set of multiscale growth patterns, in which important features of natural fracture systems are modeled including nonplanarity, segmentation, local clustering, and spanning fractures. Figure 16 shows the normalized density distributions of fracture lengths of this realization set, and it seems that the data can be fitted by a power law with an exponent $a \approx 2.6$.

Important properties of multiscale growth networks (10 realizations for each stress condition) are summarized in Table 3. Variation of fracture density caused by crack propagation is neglected due to its minor effect. Topological attributes are averaged for all realizations, while stress-dependent parameters (e.g., aperture and porosity) are listed separately for each stress scenario. Fractal dimension $D \approx 2$ over all scales indicates that the homogeneous filling feature is retained by the growth model. The networks at larger scales show relatively higher length exponent, implying the existence of certain biases tending to underestimate the existence of longer fractures under the repetitive assumption of the proposed method, which has also resulted in the scale invariance of P_{21} and intersection density ω (consequences and solutions will be discussed in section 6). Percolation parameter p increases with

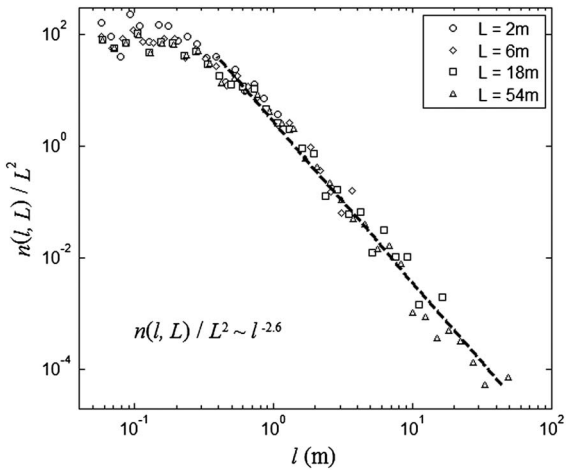

Figure 16. Normalized density distributions of fracture lengths of a realization set of multiscale growth networks.

Table 3. Properties of Multiscale Growth Network Realizations

Properties	2 m	6 m	18 m	54 m
Fractal dimension D	1.98	1.95 ± 0.04	1.97 ± 0.01	1.96 ± 0.01
Length exponent a	2.43	2.54 ± 0.11	2.59 ± 0.11	2.66 ± 0.12
Fracture intensity P_{21} (m^{-1})	10.84	10.77 ± 0.06	10.72 ± 0.07	10.68 ± 0.07
Percolation parameter p	7.48	11.32 ± 0.57	13.94 ± 0.94	14.43 ± 1.63
Maximum fracture length (m)	2.01	6.04 ± 0.00	18.11 ± 0.01	54.34 ± 0.03
Intersection density ω (m^{-2})	25.00	23.69 ± 0.59	23.72 ± 0.36	23.96 ± 0.36
		Hydrostatic Stress Condition		
Fracture porosity φ (%)	0.110	0.125 ± 0.020	0.131 ± 0.034	0.133 ± 0.035
Harmonic mean aperture (mm)	0.062	0.064 ± 0.000	0.066 ± 0.000	0.066 ± 0.001
Geometric mean aperture (mm)	0.090	0.097 ± 0.001	0.100 ± 0.001	0.101 ± 0.001
Arithmetic mean aperture (mm)	0.124	0.165 ± 0.004	0.205 ± 0.012	0.253 ± 0.026
		Deviatoric Stress Condition		
Fracture porosity φ (%)	0.160	0.229 ± 0.006	0.263 ± 0.016	0.273 ± 0.019
Harmonic mean aperture (mm)	0.058	0.063 ± 0.001	0.065 ± 0.001	0.066 ± 0.001
Geometric mean aperture (mm)	0.093	0.116 ± 0.002	0.128 ± 0.002	0.134 ± 0.002
Arithmetic mean aperture (mm)	0.166	0.296 ± 0.061	0.435 ± 0.055	0.628 ± 0.078

the system size since more large fractures are involved as a result of extrapolating censored fractures in larger domains. Rock porosity φ, defined as the fraction of aperture space over total rock volume, increases with scale as a result of scaled and coupled displacement attributes. The equivalent aperture for each fracture population is calculated using the generalized f-mean function given by

$$\overline{b}_{\mathrm{h}}^{3} = f^{-1}\left(\sum_{i=1}^{n} w_i f\left(b_{\mathrm{h}i}^{3}\right)\right) \tag{24}$$

where n is the total number of fractures, $w_i = l_i/l_{\mathrm{tot}}$ is the length-based weight of the ith fracture, $b_{\mathrm{h}i}$ is the hydraulic aperture of the ith fracture, and $f = x$, $1/x$, or $\ln(x)$ corresponds to arithmetic, harmonic, or geometric mean, respectively. Arithmetic mean treats fractures as connected in parallel and tends to give an upper bound, while harmonic mean assumes fractures as connected in series and tends to provide a lower bound [*de Marsily*, 1986; *Zimmerman and Bodvarsson*, 1996; *Ronayne and Gorelick*, 2006; *Leung and Zimmerman*, 2012]. Permeability of 2D heterogeneous media is more likely to be governed by the geometric mean of local fracture permeability that follows a lognormal or power law distribution [*de Marsily*, 1986; *de Dreuzy et al*., 2002]. The aperture of each individual fracture, that is, $b_{\mathrm{h}i}$ in equation (24), is derived as the harmonic mean of its segmental apertures since fracture segments are connected in series in the 2D scenario. Growth realizations of different stress cases are associated with a close value for harmonic mean aperture, whereas the deviatoric case shows a slightly higher geometric mean and remarkably larger arithmetic mean aperture compared to the hydrostatic case.

5.2. Flow in Multiscale Fractured Porous Rock

Fluid flow properties of the growth networks are modeled by single-phase filtration experiments based on the hybrid finite element-finite volume method [*Paluszny et al*., 2007]. Fractures are segmented into lower dimensional line elements, which are embedded in a uniform matrix material discretized by an unstructured finite element grid [*Paluszny and Matthäi*, 2010]. Matrix permeability k_{m} of fractured hydrocarbon reservoirs ranges between 1 mD and 1 D [*Matthäi and Belayneh*, 2004], and a lower bound value, that is $1\times10^{-15}\,\mathrm{m}^2$, is adopted here. Fracture permeability k_{f} is characterized using piecewise hydraulic apertures obeying the cubic law (i.e., $k_{\mathrm{f}} = b_{\mathrm{h}}^2/12$), with a harmonic mean value (lower bound) derived to be $\sim3\times10^{-10}\,\mathrm{m}^2$. In the highly connected disordered media, flow is dominated by fractures due to the large fracture-matrix permeability contrast, i.e., $k_{\mathrm{f}}/k_{\mathrm{m}} > 10^5$–$10^6$ [*Matthäi and Belayneh*, 2004]. By applying a prescribed macroscopic pressure differential on each pair of opposite boundaries, the fluid pressure and velocity fields are resolved with equivalent permeability of the differently sized domains further computed [*Lang et al*., 2014].

Figure 17 shows the permeability scaling trend of the 10 sets of growth realizations in both x and y directions (error bars represent ±1 standard deviation). It can be noted that the equivalent permeability is always at least

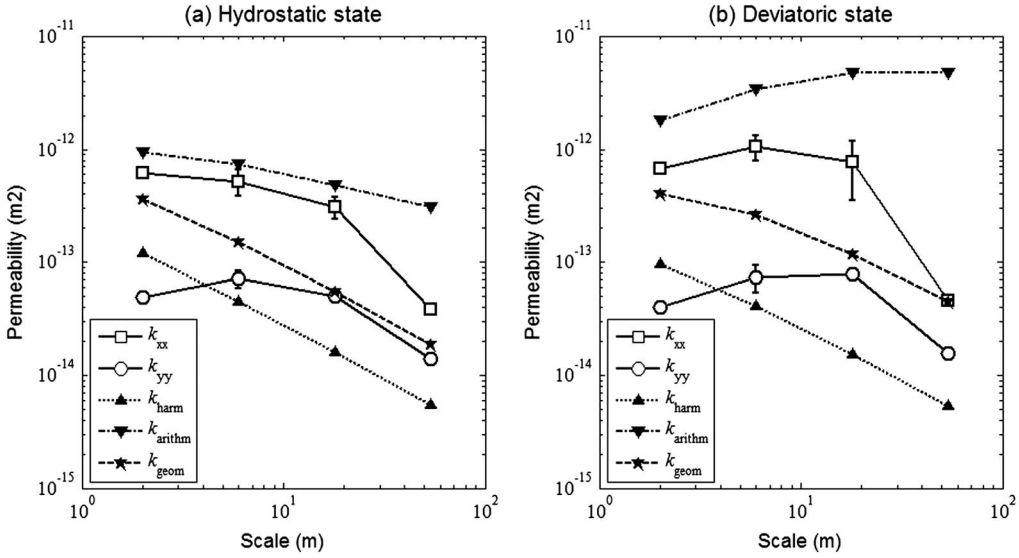

Figure 17. Equivalent permeability k_{xx} and k_{yy} computed from the flow simulation and analytical permeability k_{harm}, k_{arithm}, and k_{geom} calculated by substituting the harmonic, arithmetic, and geometric mean apertures, respectively, into Equation (25), under the applied (a) hydrostatic and (b) deviatoric stress conditions.

one order of magnitude larger than the matrix permeability (i.e., 1×10^{-15} m^2), which verifies the expected fluid partitioning behavior, that is, fracture-dominated flow. With the scale increasing, the permeability of the deviatoric case displays an upward trend at the small and intermediate scales (<10–20 m) and a continued downward trend at larger scales (>20 m), whereas the permeability of the hydrostatic case mainly shows a downward trend except a slight increase in the *y* direction at the small scale (<10 m). Fracture networks under the deviatoric condition appear to possess higher permeability due to their wider apertures.

Two factors are considered to dominate the permeability scaling trend: (i) the length exponent *a* that governs the connectivity scaling of a fracture population [*Berkowitz et al*., 2000; *Darcel et al*., 2003b] and (ii) the correlation exponents n_1 and n_2 which regulate the transmissivity scaling of each individual fracture [*de Dreuzy et al*., 2002; *Neuman*, 2008]. For the studied case of $2 < a < D+1$, with the increase of domain size L, the number of fractures larger than L (i.e., traversing fractures) increases as $\sim L^{-a+D+1}$ [*Davy et al*., 2006], whereas the relative percentage of such fractures decreases as $\sim L^{-a+D-1}$. Thus, a global downward trend might be expected for rock permeability at large scales [*Renshaw*, 1998; *Klimczak et al*., 2010]. The flow behavior is also significantly affected by the distribution of variable apertures, which leads to diversity of fluid flow structures [*de Dreuzy et al*., 2001b] and permeability scaling trends [*Klimczak et al*., 2010]. Under a higher boundary stress ratio, longer fractures play a more important role for fluid migration due to their lower resistance [*Tsang and Neretnieks*, 1998] in association with wider apertures that are correlated with fracture length. Hence, at small scales, a permeability increase occurs in the deviatoric case attributed to the considerable contribution from long fractures [*Paluszny and Matthäi*, 2010]. However, a global decreasing trend is inevitable due to the decreasing probability of traversing fractures at larger scales, with shorter fractures carrying a heavier role for fluid transport. In the hydrostatic stress case, the equivalent permeability mainly declines with increased scale, because the slightly scaled apertures with no shear-induced dilation do not endow long fractures with highly conductive capability compared to the decreased relative frequency of long fractures whose length follows the power law.

The trend of rock permeability with scale may be further explained by the flow structure transition zone between the connecting scale and the channeling scale [*de Dreuzy et al*., 2001a, 2001b; *Davy et al*., 2006]. The connecting scale L_c (or the connection length) is where the fracture network shifts from disconnected to connected, while the channeling scale ξ (i.e., the correlation length in the percolation theory) is where the flow structure transforms from extremely channeled to distributed. As shown in Figure 18, for growth networks in the deviatoric case, the connection length L_c seems to be at a scale <2 m, which is consistent

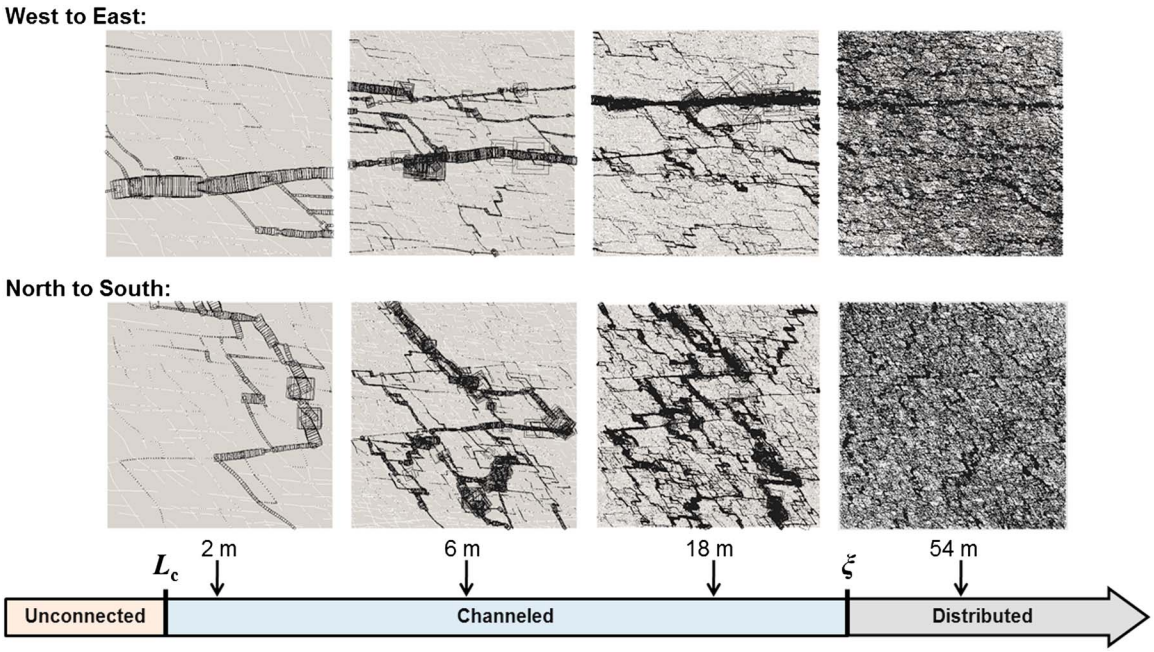

Figure 18. Flow structure transition from extremely channeled to distributed in multiscale growth networks under the deviatoric stress condition (boxes illustrate the main pathways of the flow structure).

with the predicted value of ~0.80 m in section 2.3, and the channeling scale ξ is at 20–50 m. Within the transition zone (i.e., system size from L_c to ξ), the flow structure is made up of a number of quite independent, multipath, multisegment channels [*Tsang and Neretnieks*, 1998; *de Dreuzy et al*., 2001a], under the preference of fluid to flow in least resistance paths in the disordered system of finite-sized curved fractures. This tortuosity feature has significant impact on effective flow properties [*Ronayne and Gorelick*, 2006] and may become even more crucial when the considered rock volume exceeds the channeling scale ξ, after which the percentage of domain-sized fractures decreases and flow begins to exhibit dispersive behavior, like in a homogeneous porous medium [*de Dreuzy et al*., 2001a; *Davy et al*., 2006].

For comparison with the flow modeling, an analytical solution for rock mass permeability k_{analy} can also be computed by assuming idealized orthogonal fractures fully penetrating the system domain and ignoring the flow in the matrix [*Matthäi and Belayneh*, 2004]

$$\left(L - \frac{b_h l_{tot}}{L}\right) k_{analy} = b_h \frac{b_h^2}{12} \tag{25}$$

where l_{tot} is the total length of all fractures in the $L \times L$ squared domain, b_h is the network equivalent aperture that can be substituted by the harmonic, arithmetic, or geometric mean, corresponding to the analytical permeability, k_{harm}, k_{arithm}, or k_{geom}, respectively. It is reassuring to note that the equivalent permeability is quite well bounded by the harmonic and arithmetic solutions, while the median trend is better tracked by the geometric one (Figure 17). Highly conductive fractures with long lengths and wide apertures capable of transmitting fluid across long distances seem to behave more like an "in-parallel" connected network [*Leung and Zimmerman*, 2012], so k_{xx} is better captured by the upper bound at small scales, where channels mainly constituted by very long fractures dominate the flow. However, at large scales, fluid has to migrate through less conductive branches to reach the opposite boundary due to the proportional reduction of longer fractures, which makes the fracture population act more like an "in-series" connected network and k_{xx} tends to approach the lower bound. The equivalent permeability in the y direction k_{yy} mainly exhibits closer values to the lower limit due to the inherent zigzag feature of the north-to-south flow structure. Indeed, the mechanism of network alteration from "parallel" to "series" is equivalent to the essence of flow structure transition from "channeled" to "distributed." Geometric mean seems to elegantly trace the median trend of equivalent permeability, irrespective of the anisotropic flow features, although it

cannot capture the mechanism of channeling-induced permeability increase at smaller scales. Due to the fact that the equivalent aperture of harmonic mean is not sensitive to the ratio of far-field stresses (Table 3), magnitudes of equivalent permeability under the prescribed hydrostatic and deviatoric conditions tend to converge at larger scales but with intrinsic anisotropy retained (Figure 17). At even larger scales (e.g., $>$100 m) with upscaling based on the original 2 m $\times$ 2 m source cell, the fractured rock probably behaves like a porous medium [*Long et al*., 1982] with a lower REV permeability conjectured. However, the repetition assumption might not be valid at that scale since many complex larger-scale factors (e.g., seismically visible faults, multiple rock types, and even karst features) will be involved [*Clauser*, 1992], but this is out of the scope of this paper.

6. Discussion

The stress- and scale-dependent properties of fracture attributes were modeled in this paper using the FEMDEM model for a well-interconnected fracture system. The results provide estimates of the length correlation exponents caused by fracture reactivations and interactions in response to applied stress and geomechanical constraints. The exponent n_1 for the correlation of shear displacements to fracture lengths varies from ~0.5 under a hydrostatic state to $>$1.0 under a deviatoric condition. The classical analytical solutions based on, for example, the linear elastic model [*Pollard and Segall*, 1987] or the postyield model [*Cowie and Scholz*, 1992a, 1992b] cannot fully account for the displacement-length relationship observed here. One possible reason is that these analytical formulations assume that fractures are poorly interconnected and purely straight, which oversimplifies the topological complexity of natural fracture systems involving crosscutting, segmentation, and curvature. A second is that these classical solutions apply to fractures at a critical state for propagation, which is not the general state of interest. The stress-dependent behavior of fracture apertures in this work was also captured by synthesizing both microscopic and mesoscopic effects, and a higher exponent n_2 is induced under the deviatoric stress condition. The exponent n_2 for the aperture-to-length relationship was found greatly controlled by the a priori square root correlation [*Olson*, 2003], whose universality may require further validation. Furthermore, more stress scenarios might need to be explored to examine the power law relation between aperture and length.

In the actual field measurements of a natural fracture system based on a finite-sized window sampling, observed maximum fracture length l_{max} may increase with the system size L. By assuming $n(l, L)$ ideally obeys the power law, fracture intensity P_{21} at a certain scale can be roughly calculated by substituting $l_{max} \approx L$ into equation (3):

$$P_{21}(L) \approx \frac{\alpha L^{D-2}\left(l_{min}^{-a+2} - L^{-a+2}\right)}{a-2} \tag{26}$$

which implies that P_{21} is scale dependent and increases with L for the studied scenario of $2 < a < 3$. If the domain size L is large enough, P_{21} approaches a constant value determined by l_{min}. Scale dependency of intersection density ω might also be nontrivial [*Darcel et al*., 2003b]. The proposed growth method that assumes growth cells share the same length distribution as the source cell can be seen as a first-order approximation to the real fracture system. Potentially important heterogeneity, for example, when considering a source pattern that visually seems in some ways different to the pattern in a neighbor region, cannot be accounted for in such growth models based on only one source pattern, and this source cell selection problem has already been recognized in section 3.5. When solving real problems, extraction of source patterns from different locations might be necessary, and by doing so, the lower and upper bounds of permeability may be informatively obtained based on growth modeling results from multiple sources. Discrepancy in length exponent of the multiscale growth networks may also be attributed to this space repetition hypothesis. However, such deviation is considered not to dramatically change the permeability scaling trend since length exponent is still kept in the regime of $2 < a < 3$. To more realistically model the natural heterogeneity, a tuning mechanism can be introduced by using a prescribed power law density distribution of lengths to adjust the growth results. Correlation between fracture position and length that have been reported [*Bour and Davy*, 1997; *Darcel et al*., 2003a] is also an important influence to be incorporated. Development of such modules will be the next step of this research, and a validation may be conducted based on some outcrop patterns over several scales, for example in [*Bour et al*., 2002]. Interesting directions for future work arising from this growth

methodology include modeling of networks having different fractal dimensions (e.g., $1 < D < 2$) and length exponents (e.g., $1 < a < 2$ and $a > 3$) [*de Dreuzy et al*., 2001a], development of a random walk algorithm for hierarchical patterns involving sequential formation and geological arrest [*Paluszny and Matthäi*, 2010; *Davy et al*., 2010, 2013], and upscaling realistic apertures derived from direct (two-way) hydromechanical coupling, where the effect of pore fluid pressure on aperture evolution can be dynamically captured [*Rutqvist and Stephansson*, 2003; *Vass et al*., 2014; *Ghani et al*., 2013].

Another limitation of this research is that 2D analysis was used to model the actual 3D fracture systems. The finite layer thickness may influence the fracture growth process and leads to the existence of a characteristic length that defines the transition of scaling behavior [*Bonnet et al*., 2001]. The role of bedding interfaces can also have important 3D effects on the hydromechanical behavior of the layered rock. For example, apertures vary considerably for extensional layer-normal joints affected by delamination or variable interface slip. Fractures may propagate across the bedding interface, depending on layer mechanical properties, local stress fields, and finite strains. Potentially dominant role of flow in the bedding planes due to delamination between the limestone and the shales and focused flows in such crosscutting fractures may also be essential. To achieve 3D geomechanical modeling, a newly developed 3D crack propagation model [*Guo et al*., 2014] will be employed to capture the brittle deformation response including local concentrations of critically high tensile or differential stresses, together with realistic fracture opening and shearing behavior on both preexisting and newly propagated fractures. Such capability opens the way to modeling 3D flows in geomechanically realistic fractured layers as well as channelized flow in comminuted fracture intersections and bedding planes, based on which a 3D network upscaling method can be further developed to statistically estimate rock mass properties in larger scales.

7. Conclusions

To conclude, in the scope of 2D analysis, a new methodology has been developed for upscaling fracture network models while preserving geostatistical and geomechanical characteristics. Four main parts were undertaken in this research:

1. The scaling properties of an outcrop sample were quantitatively interpreted in terms of spatial organization, lengths, connectivity, and displacements using methodologies that employ power law and fractal geometry assumptions. The fracture pattern is observed to be nonfractal with the fractal dimension $D \approx 2$, while its length distribution follows a power law with the exponent $2 < a < 3$. These coefficients are further exploited by the new main aspect of the methodology—the application of the random walk method.
2. Realistic distributions of fracture apertures and shear displacements were obtained for the outcrop sample, where current computational power allows resolving FEMDEM geomechanical problems with acceptable accuracy and precision. Stress-dependent correlations of displacement attributes to fracture lengths are established, and these are used to preserve the geomechanical characteristics as the network is upscaled.
3. A novel approach accommodating discrete-time random walkers in recursive growth lattices was developed to extrapolate the geologically obtained fracture pattern together with its stress- and scale-dependent displacement attributes into larger scales obeying a self-referencing scheme. Advantages of this growth approach include preserving curvature of natural cracks, capturing existence of long fractures, retaining realism of variable apertures, and respecting stress dependency of scaling laws. Validity of growth realizations was examined based on a comparison with a larger analogue system from the field with respect to its geometric properties. Scaling behavior of the new "multiscale growth" models was further justified by the agreement in fractal dimension and length power law trend.
4. Hydraulic properties of multiscale growth patterns were modeled by single-phase flow simulation, where a lower bound value for matrix permeability was adopted to achieve fracture-dominated flow. Distinct permeability scaling trends were discerned in the disordered geologic media associated with different geomechanical constraints. A transition zone was inferred to be occurring when the flow structure shifts from extremely channeled to distributed, tending to be more governed by diffusive processes at even larger scales. Analysis based on an analytical model reveals an equivalent network alteration from "parallel" (where arithmetic mean is more applicable) to "series" (where harmonic mean is more applicable).

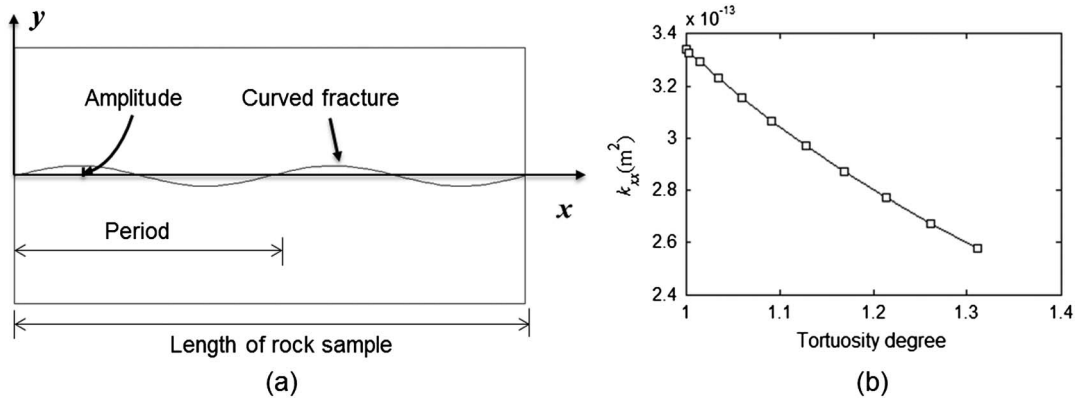

Figure A1. (a) Single curved fracture model with assumed sinusoidal shapes and (b) variation of rock sample permeability in the *x* direction as a function of tortuosity degree.

Furthermore, the median trend of equivalent permeability irrespective of inherent anisotropy was found to be well tracked by geometric mean.

The observed stress effects on the scaling behavior of fracture attributes and rock permeability suggest the importance of incorporating geomechanical analysis for a more meaningful scheme when upscaling network models for reservoir simulation.

Appendix A

Effect of fracture curvature is examined based on a series of single-fracture models with assumed sinusoidal shapes (Figure A1a). The length of the rock sample is 0.5 m, and the amplitude of each sinusoidal curve is fixed to be 0.01 m. Curvature is modeled by changing the number of waving periods from 0 (straight line) to 10, and the degree of tortuosity is measured as the ratio of total arc length of each sinusoidal curve to the rock sample length (i.e., 0.5 m). A constant aperture value of 0.1 mm is assigned for each curved fracture. Single-phase fluid flow is conducted by applying a pressure differential between left and right boundaries and no-flow conditions on the top and bottom boundaries. As shown in Figure A1b, the permeability of the rock sample in the *x* direction decreases with the increase of tortuosity degree following a nonlinear trend. The results imply that fracture curvature may have an important influence on the fracture transmissivity, depending on the degree of tortuosity.

Acknowledgments
The authors would like to thank the sponsors of the itf-ISF project "Improved Simulation of Faulted and Fractured Reservoirs" and to acknowledge the Janet Watson scholarship, awarded to the first author by the Department of Earth Science and Engineering, Imperial College London. We thank Philippe Davy and Renaud Toussaint for their very constructive reviews. Data supporting this article are available for sharing and can be obtained by contacting the corresponding author Qinghua Lei (q.lei12@imperial.ac.uk).

References

Asadollahi, P., and F. Tonon (2010), Constitutive model for rock fractures: Revisiting Barton's empirical model, *Eng. Geol.*, *113*, 11–32, doi:10.1016/j.enggeo.2010.01.007.

Baghbanan, A., and L. Jing (2008), Stress effects on permeability in a fractured rock mass with correlated fracture length and aperture, *Int. J. Rock Mech. Min. Sci.*, *45*, 1320–1334, doi:10.1016/j.ijrmms.2008.01.015.

Bandis, S. C., A. C. Lumsden, and N. R. Barton (1983), Fundamentals of rock joint deformation, *Int. J. Rock Mech. Min. Sci. Geomech. Abstr.*, *20*(6), 249–268, doi:10.1016/0148-9062(83)90595-8.

Barton, C. C., and P. R. La Pointe (1995), *Fractals in the Earth Sciences*, Plenum Press, New York.

Barton, N. (1981), Some size dependent properties of joints and faults, *Geophys. Res. Lett.*, *8*(7), 667–670, doi:10.1029/GL008i007p00667.

Barton, N., S. C. Bandis, and K. Bakhtar (1985), Strength, deformation and conductivity coupling of rock joints, *Int. J. Rock Mech. Min. Sci. Geomech. Abstr.*, *22*(3), 121–140, doi:10.1016/0148-9062(85)93227-9.

Belayneh, M. W., S. K. Matthäi, M. J. Blunt, and S. F. Rogers (2009), Comparison of deterministic with stochastic fracture models in water-flooding numerical simulations, *AAPG Bull.*, *93*(11), 1633–1648, doi:10.1306/07220909031.

Berkowitz, B., and A. Hadad (1997), Fractal and multifractal measures of natural and synthetic fracture networks, *J. Geophys. Res.*, *102*(B6), 12,205–12,218, doi:10.1029/97JB00304.

Berkowitz, B., O. Bour, P. Davy, and N. Odling (2000), Scaling of fracture connectivity in geological formations, *Geophys. Res. Lett.*, *27*(14), 2061–2064, doi:10.1029/1999GL011241.

Bonnet, E., O. Bour, N. E. Odling, P. Davy, I. Main, P. Cowie, and B. Berkowitz (2001), Scaling of fracture systems in geological media, *Rev. Geophys.*, *39*(3), 347–383, doi:10.1029/1999RG000074.

Bour, O., and P. Davy (1997), Connectivity of random fault networks following a power law fault length distribution, *Water Resour. Res.*, *33*(7), 1567–1583, doi:10.1029/96WR00433.

Bour, O., and P. Davy (1999), Clustering and size distribution of fault patterns: Theory and measurements, *Geophys. Res. Lett.*, *26*(13), 2001–2004, doi:10.1029/1999GL900419.

Bour, O., P. Davy, and C. Dacel (2002), A statistical scaling model for fracture network geometry, with validation on a multiscale mapping of a joint network (Hornelen Basin, Norway), *J. Geophys. Res.*, *107*(B6), 2113, doi:10.1029/2001JB000176.

Brace, W. F. (1980), Permeability of crystalline and argillaceous rocks, *Int. J. Rock Mech. Min. Sci. Abstr.*, *17*, 241–251, doi:10.1016/0148-9062(80)90807-4.

Brace, W. F. (1984), Permeability of crystalline rocks: New in situ measurements, *J. Geophys. Res.*, *89*(B6), 4327–4330, doi:10.1029/JB089iB06p04327.
Chilès, J. P. (1988), Fractal and geostatistical methods for modeling of a fracture network, *Math. Geol.*, *20*, 631–654.
Clauser, C. (1992), Permeability of crystalline rocks, *Eos Trans. AGU*, *73*(21), 233–238, doi:10.1029/91EO00190.
Cowie, P. A., and C. H. Scholz (1992a), Physical explanation for the displacement-length relationship of faults using a post-yield fracture mechanics model, *J. Struct. Geol.*, *14*(10), 1133–1148, doi:10.1016/0191-8141(92)90065-5.
Cowie, P. A., and C. H. Scholz (1992b), Displacement-length scaling relationship for faults: Data synthesis and discussion, *J. Struct. Geol.*, *14*(10), 1149–1156, doi:10.1016/0191-8141(92)90066-6.
Darcel, C., O. Bour, and P. Davy (2003a), Cross-correlation between length and position in real fracture networks, *Geophys. Res. Lett*, *30*(12), 1650, doi:10.1029/2003GL017174.
Darcel, C., O. Bour, P. Davy, and J.-R. de Dreuzy (2003b), Connectivity properties of two-dimensional fracture networks with stochastic fractal correlation, *Water Resour. Res.*, *39*(10), 1272, doi:10.1029/2002WR001628.
Davy, P. (1993), On the frequency-length distribution of the San Andreas fault system, *J. Geophys. Res.*, *98*(B7), 12,141–12,151, doi:10.1029/93JB00372.
Davy, P., O. Bour, J.-R. de Dreuzy, and C. Darcel (2006), Flow in multiscale fractal fracture networks, *Geol. Soc. London Spec. Publ.*, *261*, 31–45, doi:10.1144/GSL.SP.2006.261.01.03.
Davy, P., R. Le Goc, C. Darcel, O. Bour, J.-R. de Dreuzy, and R. Munier (2010), A likely universal model of fracture scaling and its consequence for crustal hydromechanics, *J. Geophys. Res.*, *115*, B10411, 2010, doi:10.1029/2009JB007043.
Davy, P., R. Le Goc, and C. Darcel (2013), A model of fracture nucleation, growth and arrest, and consequences for fracture density and scaling, *J. Geophys. Res. Solid Earth*, *118*, 1393–1407, doi:10.1002/jgrb.50120.
Dawers, N. H., M. H. Anders, and C. H. Scholz (1993), Growth of normal faults: Displacement-length scaling, *Geology*, *21*, 1107–1110, doi:10.1130/0091-7613(1993)021<1107:GONFDL>2.3.CO;2.
de Dreuzy, J.-R., P. Davy, and O. Bour (2001a), Hydraulic properties of two-dimensional random fracture networks following a power law length distribution: 1. Effective connectivity, *Water Resour. Res.*, *37*(8), 2065–2078, doi:10.1029/2001WR900011.
de Dreuzy, J.-R., P. Davy, and O. Bour (2001b), Hydraulic properties of two-dimensional random fracture networks following a power law length distribution: 2. Permeability of networks based on log-normal distribution of apertures, *Water Resour. Res.*, *37*(8), 2079–2095, doi:10.1029/2001WR900010.
de Dreuzy, J.-R., P. Davy, and O. Bour (2002), Hydraulic properties of two-dimensional random fracture networks following power law distributions of length and aperture, *Water Resour. Res. 38*(12), 1276, doi:10.1029/2001WR001009.
de Marsily, G. (1986), *Quantitative Hydrogeology: Groundwater Hydrology for Engineers*, Academic Press, Orlando.
Fossen, H., and J. Hesthammer (1997), Geometric analysis and scaling relations of deformation bands in porous sandstone, *J. Struct. Geol.*, *19*, 1479–1493, doi:10.1016/S0191-8141(97)00075-8.
Ghani, I., D. Koehn, R. Toussaint, and C. W. Passchier (2013), Dynamic development of hydrofracture, *Pure Appl. Geophys.*, *170*(11), 1685–1703, doi:10.1007/s00024-012-0637-7.
Gillespie, P. A., J. J. Walsh, and J. Watterson (1992), Limitations of dimension and displacement data from single faults and the consequences for data analysis and interpretation, *J. Struct. Geol.*, *14*(10), 1157–1172, doi:10.1016/0191-8141(92)90067-7.
Guo, L., J.-P. Latham, and J. Xiang (2014), Numerical simulation of breakages of concrete armour units using a three-dimensional fracture model in the context of the combined finite-discrete element method, *Comput. Struct.*, *146*, 117–142, doi:10.1016/j.compstruc.2014.09.001.
Hatton, C. G., I. G. Main, and P. G. Meredith (1994), Non-universal scaling of fracture length and opening displacement, *Nature*, *367*, 160–162, doi:10.1038/367160a0.
Hentschel, H. G. E., and I. Procaccia (1983), The infinite number of generalized dimensions of fractals and strange attractors, *Physica*, *8D*, 435–444.
Kaye, B. H. (1994), *A Random Walk Through Fractal Dimensions*, Weinheim, VCH.
Kim, Y.-S., and D. J. Sanderson (2005), The relationship between displacement and length of faults: A review, *Earth Sci. Rev.*, *68*, 317–334, doi:10.1016/j.earscirev.2004.06.003.
Klimczak, C., R. A. Schultz, R. Parashar, and D. M. Reeves (2010), Cubic law with aperture-length correlation: Implications for network scale fluid flow, *Hydrogeol. J.*, *18*(4), 851–862, doi:10.1007/s10040-009-0572-6.
Lama, R. D., and V. S. Vutukuri (1978), *Handbook on Mechanical Properties of Rocks: Testing Techniques and Results*, vol. II, Trans Tech Publications, Clausthal, Germany.
Lang, P. S., A. Paluszny, and R. W. Zimmerman (2014), Permeability tensor of three-dimensional fractured porous rock and a comparison to trace map predictions, *J. Geophys. Res. Solid Earth*, *199*, 6288–6307, doi:10.1002/2014JB011027.
Latham, J.-P., J. Xiang, M. W. Belayneh, H. M. Nick, C.-F. Tsang, and M. J. Blunt (2013), Modelling stress-dependent permeability in fractured rock including effects of propagating and bending fractures, *Int. J. Rock Mech. Min. Sci.*, *57*, 100–112, doi:10.1016/j.ijrmms.2012.08.002.
Lei, Q., J.-P. Latham, J. Xiang, C.-F. Tsang, P. Lang, and L. Guo (2014), Effects of geomechanical changes on the validity of a discrete fracture network representation of a realistic two-dimensional fractured rock, *Int. J. Rock Mech. Min. Sci.*, *70*, 507–523, doi:10.1016/j.ijrmms.2014.06.001.
Lei, Q., J.-P. Latham, J. Xiang, and C.-F. Tsang (2015), Polyaxial stress-induced variable aperture model for persistent 3D fracture networks, *Geomech. Energy Environ.*, *1*, 34–47, doi:10.1016/j.gete.2015.03.003.
Leung, C. T. O., and R. W. Zimmerman (2012), Estimating the hydraulic conductivity of two-dimensional fracture networks using network geometric properties, *Transp. Porous Media*, *93*, 777–797, doi:10.1007/s11242-012-9982-3.
Long, J. C. S., J. S. Remer, C. R. Wilson, and P. A. Witherspoon (1982), Porous media equivalents for networks of discontinuous fractures, *Water Resour. Res.*, *18*(3), 645–658, doi:10.1029/WR018i003p00645.
Mahabadi, O. K., B. S. A. Tatone, and G. Grasselli (2014), Influence of microscale heterogeneity and microstructure on the tensile behavior of crystalline rocks, *J. Geophys. Res. Solid Earth*, *119*, 5324–5341, doi:10.1002/2014JB011064.
Mandelbrot, B. B. (1982), *The Fractal Geometry of Nature*, WH Freeman, New York.
Matthäi, S. K., and M. Belayneh (2004), Fluid flow partitioning between fractures and a permeable rock matrix, *Geophys. Res. Lett.*, *31*, L07602, doi:10.1029/2003GL019027.
Min, K. B., J. Rutqvist, C.-F. Tsang, and L. Jing (2004), Stress dependent permeability of fractured rock masses: A numerical study, *Int. J. Rock Mech. Min. Sci.*, *41*, 1191–1210, doi:10.1016/j.ijrmms.2004.05.005.
Munjiza, A. (2004), *The Combined Finite-Discrete Element Method*, John Wiley, London.
Munjiza, A., E. E. Knight, and E. Rougier (2011), *Computational Mechanics of Discontinua*, John Wiley, Chichester.

Neuman, S. P. (1994), Generalized scaling of permeabilities: Validation and effect of support scale, *Geophys. Res. Lett.*, *21*(5), 349–352, doi:10.1029/94GL00308.
Neuman, S. P. (2008), Multiscale relationships between fracture length, aperture, density and permeability, *Geophys. Res. Lett.*, *35*, L22402, doi:10.1029/2008GL035622.
Odling, N. E. (1992), Network properties of a two-dimensional natural fracture pattern, *Pure Appl. Geophys.*, *138*(1), 95–114, doi:10.1007/BF00876716.
Odling, N. E. (1997), Scaling and connectivity of joint systems in sandstones from western Norway, *J. Struct. Geol.*, *19*(10), 1257–1271, doi:10.1016/S0191-8141(97)00041-2.
Olson, J. E. (2003), Sublinear scaling of fracture aperture versus length: An exception or the rule?, *J. Geophys. Res.*, *108*(B9), 2413, doi:10.1029/2001JB000419.
Olsson, R., and N. Barton (2001), An improved model for hydromechanical coupling during shearing of rock joints, *Int. J. Rock Mech. Min. Sci.*, *38*, 317–329, doi:10.1016/S1365-1609(00)00079-4.
Paluszny, A., and S. K. Matthäi (2010), Impact of fracture development on the effective permeability of porous rocks as determined by 2-D discrete fracture growth modelling, *J. Geophys. Res.*, *115*, B02203, doi:10.1029/2008JB006236.
Paluszny, A., S. K. Matthäi, and M. Hohmeyer (2007), Hybrid finite element finite volume discretization of complex geologic structures and a new simulation workflow demonstrated on fractured rocks, *Geofluids*, *7*, 186–208, doi:10.1111/j.1468-8123.2007.00180.x.
Pickering, G., J. M. Bull, and D. J. Sanderson (1995), Sampling power-law distributions, *Tectonophysics*, *248*, 1–20, doi:10.1016/0040-1951(95)00030-Q.
Pollard, D. D., and P. Segall (1987), Theoretical displacements and stresses near fractures in rock: With applications to faults, joints, veins, dikes, and solution surfaces, in *Fracture Mechanics of Rock*, edited by B. K. Atkinson, pp. 277–350, Academic Press, San Diego, Calif.
Renshaw, C. E. (1998), Sample bias and the scaling of hydraulic conductivity in fractured rock, *Geophys. Res. Lett.*, *25*(1), 121–124, doi:10.1029/97GL03400.
Renshaw, C. E., and J. C. Park (1997), Effect of mechanical interactions on the scaling of fracture length and aperture, *Nature*, *386*, 482–484, doi:10.1038/386482a0.
Ronayne, M. J., and S. M. Gorelick (2006), Effective permeability of porous media containing branching channel networks, *Phys. Rev. E*, *73*, 026305, doi:10.1103/PhysRevE.73.026305.
Roy, A., E. Perfect, W. M. Dunne, and L. D. McKay (2007), Fractal characterization of fracture networks: An improved box-counting technique, *J. Geophys. Res.*, *112*, B112201, doi:10.1029/2006JB004582.
Rutqvist, J., and O. Stephansson (2003), The role of hydromechanical coupling in fractured rock engineering, *Hydrogeol. J.*, *11*(1), 7–40, doi:10.1007/s10040-002-0241-5.
Scholz, C. H., N. H. Dawers, J.-Z. Yu, M. H. Anders, and P. A. Cowie (1993), Fault growth and fault scaling laws: Preliminary results, *J. Geophys. Res.*, *98*(B12), 21,951–21,961, doi:10.1029/93JB01008.
Schultz, R. A., R. Soliva, H. Fossen, C. H. Okubo, and D. M. Reeves (2008), Dependence of displacement-length scaling relations for fractures and deformation bands on the volumetric changes across them, *J. Struct. Geol.*, *30*, 1405–1411, doi:10.1016/j.jsg.2008.08.001.
Tsang, C.-F., and I. Neretnieks (1998), Flow channeling in heterogeneous fractured rocks, *Rev. Geophys.*, *36*(2), 275–298, doi:10.1029/97RG03319.
Vass, A., D. Koehn, R. Toussaint, I. Ghani, and S. Piazolo (2014), The importance of fracture-healing on the deformation of fluid-filled layered systems, *J. Struct. Geol.*, *67*, 94–106, doi:10.1016/j.jsg.2014.07.007.
Vermilye, J. M., and C. H. Scholz (1995), Relation between vein length and aperture, *J. Struct. Geol.*, *17*(3), 423–434, doi:10.1016/0191-8141(94)00058-8.
Walmann, T., A. Malthe-Sørenssen, J. Feder, T. Jøssang, P. Meakin, and H. H. Hardy (1996), Scaling relations for the lengths and widths of fractures, *Phys. Rev. Lett.*, *77*, 5393–5396, doi:10.1103/PhysRevLett.77.5393.
Walsh, J. J., and J. Watterson (1988), Analysis of the relationship between displacements and dimensions of faults, *J. Struct. Geol.*, *10*, 239–247, doi:10.1016/0191-8141(88)90057-0.
Walsh, J. J., and J. Watterson (1993), Fractal analysis of fracture patterns using the standard box-counting technique: Valid and invalid methodologies, *J. Struct. Geol.*, *15*(12), 1509–1512, doi:10.1016/0191-8141(93)90010-8.
Xiang, J., A. Munjiza, J.-P. Latham, and R. Guises (2009), Finite strain, finite rotation quadratic tetrahedral element for the combined finite-discrete element method, *Int. J. Numer. Methods Eng.*, *79*, 946–978, doi:10.1002/nme.2599.
Zimmerman, R. W., and G. S. Bodvarsson (1996), Effective transmissivity of two-dimensional fracture networks, *Int. J. Rock Mech. Min. Sci. Abstr.*, *33*(4), 433–438, doi:10.1016/0148-9062(95)00067-4.
Zimmerman, R. W., and I. Main (2004), Hydromechanical behavior of fractured rocks, in *Mechanics of Fluid-Saturated Rocks*, edited by Y. Gueguen and M. Bouteca, pp. 363–421, Elsevier, London.